J. Fluid Mech. (2008), *vol.* 600, *pp.* 133–165.
doi:10.1017/S002211200800030X Printed in the United Kingdom

Unsteady flows in pipes with finite curvature

J. H. SIGGERS[1] AND S. L. WATERS[2]†

[1]Department of Bioengineering, Imperial College London, London, SW7 2AZ, UK

[2]Oxford Centre for Industrial & Applied Mathematics, Mathematical Institute, 24–29 St Giles', Oxford University, Oxford, OX2 6HS, UK

(Received 24 January 2007 and in revised form 16 December 2007)

Motivated by the study of blood flow in a curved artery, we consider fluid flow through a curved pipe of uniform curvature, δ, driven by a prescribed oscillatory axial pressure gradient. The curved pipe has finite (as opposed to asymptotically small) curvature, and we determine the effects of both the centrifugal and Coriolis forces on the flow. In addition to δ, the flow is parameterized by the Dean number, D, the Womersley number, α, and a secondary streaming Reynolds number, R_s. Asymptotic solutions are developed for the case when $\delta \ll 1$, $\alpha \ll 1$ and the magnitude of the axial pressure gradient is small, using regular perturbation techniques. For intermediate values of the governing parameters, a pseudospectral code is used to obtain numerical solutions. For flows driven by a sinusoidal pressure gradient ($D = 0$), we identify three distinct classes of stable solutions: 2π-periodic symmetric, 2π-periodic asymmetric, and asymmetric solutions that are either quasi-periodic, or periodic with period $2\pi k$ for $k \in \mathbb{N}$. The transition between solutions is dependent on the value of δ; thus pipes with finite curvature may exhibit qualitatively different transitions between the solution classes as the governing parameters are varied from those of curved pipes with asymptotically small curvature. When $\alpha \gg 1$, matched asymptotic expansions are used to simplify the system, and the resulting equations are solved analytically for $R_s \ll 1$, $\delta \ll 1$ and numerically for larger parameter values. We then determine the effect of a non-zero steady component of the pressure gradient ($D \neq 0$), and show that, for certain parameter values, when D is above a critical value the periodic asymmetric solutions regain spatial symmetry. Finally, we show that the effects of finite curvature can lead to substantial quantitative differences in the wall shear stress distribution and discuss briefly the physiological implications of the results for blood flow in arteries.

1. Introduction

Fluid flow in a curved pipe has many applications to physiological fluid flows and industrial fluid dynamics. Our main motivation is blood flow in arteries. Atherosclerosis is the most common arterial disease, and it is now widely accepted that the spatial distribution of atherosclerotic plaques, which characterize the disease, is correlated with the distribution of arterial wall shear stress (WSS) (Caro, FitzGerald & Schroter 1971). In particular, plaques tend to develop in regions of low mean WSS and regions where the WSS changes direction in the course of the cardiac cycle.

† Author to whom correspondence should be addressed: waters@maths.ox.ac.uk

Atherosclerosis leads to ischaemic symptoms through the gradual restriction of blood flow as the plaques occupy progressively more of the arterial lumen. An additional health risk is the vulnerability of the plaque to rupture or erosion, which can, in turn, give rise to thromboses. Emboli may then break off and be carried downstream and block smaller vessels.

To provide insight into the sites at which plaques develop, many studies have considered fluid flow in an arterial model. Two main approaches are adopted. The first approach aims to replicate a realistic artery from patient data and study the fluid flows using full CFD simulations (see for example Steinman (2002) and references therein). This approach is patient-specific and reveals the exact quantitative nature of the flow properties. A complementary approach is to idealize the problem, for example by considering a simplified arterial geometry and form of the driving pressure, and significantly more physical insight into the underlying mechanisms can be obtained than by computational simulation of the full system alone. We adopt this approach here.

We model the artery as a pipe with constant circular cross-section of radius a, having a centreline lying on an arc of a circle of radius R. The dimensionless curvature ratio of the pipe is $\delta = a/R$. The blood is modelled as a Newtonian viscous fluid driven by an oscillatory axial pressure gradient of the form $-P_0 - K\cos(t)$, where $-P_0$ is the steady component, K is the amplitude of the sinusoidal component, and time, t, has been non-dimensionalized by T, where $2\pi T$ is the period of the sinusoidal component of the pressure gradient. Throughout this paper we use the term oscillatory to refer to pressure gradients of the form $-P_0 - K\cos t$ and sinusoidal to refer to pressure gradients of the form $-K\cos t$. In addition to the curvature, δ, the flow is characterized by three dimensionless parameters: (i) the Dean number, $D = 4Re\sqrt{2\delta}$, where Re is the Reynolds number based on the maximum axial velocity of the flow that would be driven by the steady component of the pressure gradient in a straight pipe of radius a; (ii) the Womersley parameter, $\alpha = (a^2/\nu T)^{1/2}$, where ν is the kinematic viscosity of the fluid, and α^2 is equal to the ratio of the time scale for viscous diffusion of momentum across the pipe to the period of the pressure gradient oscillations; and (iii) the secondary streaming Reynolds number R_s, which is a Reynolds number based on the scale of the secondary velocity generated (the velocity in the plane of cross-section of the pipe), when the flow is driven by a sinusoidal pressure gradient.

In this paper we consider fully developed flows driven by oscillatory and sinusoidal pressure gradients. For flows driven by steady pressure gradients see Pedley (1980), Berger, Talbot & Yao (1983), Ito (1987), Siggers & Waters (2005) and references therein. The majority of previous studies of flows driven by oscillatory pressure gradients in fixed curved tubes have considered only weakly curved pipes of circular cross-section. This corresponds to taking the limit $\delta \to 0$ after having rescaled the governing equations so that only the leading-order centrifugal effects of curvature are retained.

Fully developed flow driven by a sinusoidal pressure gradient in a weakly curved pipe has been considered by a number of authors (Stuart 1966; Lyne 1971). The flow depends on R_s and α, and, for sufficiently large values of α, the flow consists of a Stokes boundary layer surrounding an inviscid core flow. Within the Stokes layer, secondary motions are generated by the nonlinear centrifugal force terms. These secondary motions have a non-zero mean, which does not tend to zero at the edge of the boundary layer, and thus drives a (two-vortex) steady secondary streaming flow in the core of the pipe. This steady streaming is parameterized by R_s, and its

direction is opposite to that for steady Dean flow. For small R_s, a series solution can be found, and for larger R_s, the solution may be found numerically (Haddon 1982; van Meerveld & Waters 2001). For asymptotically large R_s, Lyne (1971) and Stuart (1966) predicted that additional boundary layers will form around the edges and across the centreline of the pipe, both of thickness $O(aR_s^{-1/2})$; this prediction was confirmed numerically in van Meerveld & Waters (2001).

Mullin & Greated (1980) also performed a theoretical and experimental investigation of fully developed flows in weakly curved pipes, driven by a sinusoidal pressure gradient, and found a series solution for small values of an amplitude parameter (which is proportional to the square of the amplitude of the applied pressure gradient) in terms of a Hankel transform. The series solution is valid for all values of α. In the low-frequency limit, $\alpha \ll 1$, a further expansion was used and closed-form solutions were presented, which correspond to quasi-steady Dean flow. At intermediate values of α, the steady secondary flow streamline pattern has a four-vortex structure.

Fully developed flows driven by an oscillatory pressure gradient in a weakly curved pipe have also been investigated (Smith 1975; Blennerhassett 1976). Smith (1975) examined the nature of the flow when the parameters D or α are asymptotically small or large (and $R_s = O(1)$). The analysis revealed a number of pulsatile motions, and in certain cases interactions between steady boundary layers and Stokes layers were involved. Blennerhassett (1976) performed both numerical and asymptotic analyses and obtained the key result that a sinusoidal pressure gradient, composed of oscillations of more than one frequency, can result in the generation of a mean axial flow along the pipe.

The small curvature limit leads to a considerable simplification of the governing equations. However, many arteries have a significant curvature (e.g. the aortic arch has curvature ratio approximately 1/4, Chang & Tarbell 1985). There have been a number of numerical studies of flows in pipes with finite curvature (Chang & Tarbell 1985; Hamakiotes & Berger 1990; Sudo, Sumida & Yamane 1992; Tada, Oshima & Yamane 1996). Although some of these studies varied δ between the different simulations, none of them commented on the effects of varying δ. Furthermore, the studies all imposed symmetry across the centreplane of the pipe (the plane containing the centreline of the pipe), so that asymmetric solutions were not permitted. Periodic flows in curved pipes have also been investigated experimentally (Lin & Tarbell 1980; Sudo *et al.* 1992; Swanson, Stalp & Donnelly 1993; Chandran, Yearwood & Wieting 1979). While the above studies all considered curved pipes with zero torsion (so that the pipe centreline remained in the plane), flow in helical pipes has also been considered. In particular, Zabielski & Mestel (1998*a*, *b*) considered both steady and unsteady fully developed flows in helically symmetric pipes, and retained the effects of finite curvature.

In this paper we consider fully developed flow through a curved pipe of uniform curvature, δ, driven by a prescribed axial pressure gradient. The curved pipe has finite (as opposed to asymptotically small) curvature; however, we are restricted to small (but finite) curvature, since a long entry length is required to ensure fully developed flow, which is not possible for larger values of δ. We consider values of δ between 0 and 0.3, and determine the effects of both the centrifugal and Coriolis forces on the flow. Furthermore, we do not assume symmetry in the pipe centreplane (Winters 1987). In § 2, we give the governing equations. The problem is governed by the four dimensionless parameters δ, D, α and R_s. In § 3, we use regular perturbation techniques to find a series solution to the governing equations

in the limit in which both the steady component (characterized by D) and amplitude of the sinusoidal component (characterized by $R_s^{1/2}\alpha^3$) of the pressure gradient are asymptotically small, and additionally $\delta \ll 1$ and $\alpha \ll 1$. In § 4, we consider larger parameter values, and present highlights of our numerical solutions in the case of a sinusoidal pressure gradient ($D = 0$). A pseudospectral code is used to solve the governing equations, the numerical method is described in detail in § 4.1 and numerical solutions are presented in § 4.2. Three distinct classes of stable solutions are found: symmetric and 2π-periodic, asymmetric and 2π-periodic, and asymmetric solutions that are either quasi-periodic, or periodic with period $2k\pi$ for $k \in \mathbb{N}$. The transition between solutions is dependent on the value of δ; we show that pipes with finite curvature may exhibit qualitatively different transitions between the solution classes as the governing parameters are varied compared to weakly curved pipes. The numerical results show that as α increases, the flow consists of an inviscid core surrounded by a viscous Stokes boundary layer. In § 4.3, we consider asymptotically large values of α, and generalize the analysis of Lyne (1971) and Stuart (1966) to curved pipes with finite curvature using matched asymptotic expansions. The core flow is governed by R_s and δ; for small R_s and δ, we find a series solution using regular perturbation techniques, and we also present numerical solutions for larger values of these parameters. In § 5, we consider flows driven by an oscillatory pressure gradient ($D \neq 0$) and present examples of the typical flows found. Here again, we drop the assumption that the governing dimensionless parameters are asymptotically small, and the governing equations are solved using the numerical method described in § 4.1. In particular, we show an example of an asymmetric solution found in § 4.2 regaining spatial symmetry as D is increased. In § 6, we determine the behaviour of the WSS distribution as δ increases for cases of both sinusoidal and oscillatory pressure gradients. Finally, in § 7 we discuss briefly the physiological implications of our results.

2. Governing equations and parameters

The artery is modelled as a rigid-walled pipe of uniform circular cross-section with radius a. The centreline of the pipe is assumed to lie on the arc of a circle of radius R (so that torsion effects are neglected) and we define the curvature ratio $\delta = a/R \in [0, 1]$. The blood is modelled as a homogeneous incompressible viscous Newtonian fluid of density ρ and kinematic viscosity ν.

A curvilinear coordinate system (ar, θ, as) is chosen, where (ar, θ) are polar coordinates in the plane of cross-section of the pipe, and as is the distance along the centreline, as shown in figure 1. The unit vectors $(\boldsymbol{e}_r, \boldsymbol{e}_\theta, \boldsymbol{e}_s)$ denote the coordinate directions. The pipe wall is at $r = 1$, the velocity components are $U\boldsymbol{u} = U(u, v, w/\sqrt{2\delta})$ and $\rho U^2 p$ is the pressure, where $U = \nu/a$ is the velocity scale (Truesdell & Adler 1970). Note that the axial velocity scale ensures that the centrifugal force terms in the governing equations are formally of the same order as the viscous and inertial terms in the limit $\delta \to 0$. Time is given by Tt where $2\pi T$ is the period of the sinusoidal component of the pressure gradient.

The flow is driven by a prescribed dimensional oscillatory axial pressure gradient of the form $-P_0 - K\cos t$, where $-P_0$ is the steady component and K the amplitude of the sinusoidal component, respectively.

We consider only fully developed flow by neglecting derivatives of the dependent variables with respect to s. The governing equations are then (Pedley 1980):

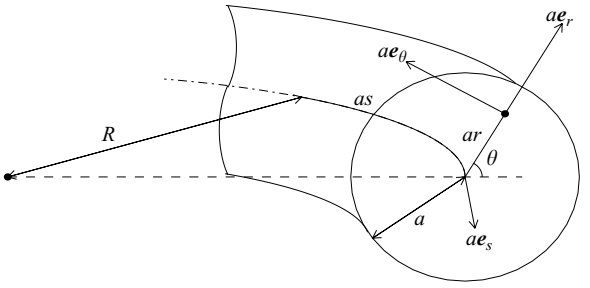

FIGURE 1. The curvilinear coordinate system.

Continuity:

$$\frac{\partial u}{\partial r}+\frac{u}{r}+\frac{1}{r}\frac{\partial v}{\partial \theta}+\frac{\delta\cos\theta}{h}u-\frac{\delta\sin\theta}{h}v=0, \tag{2.1}$$

$\boldsymbol{e}_r$:

$$\alpha^2\frac{\partial u}{\partial t}+u\frac{\partial u}{\partial r}+\frac{v}{r}\frac{\partial u}{\partial \theta}-\frac{v^2}{r}-\frac{\cos\theta}{2h}w^2=-\frac{\partial p}{\partial r}-\frac{1}{hr}\frac{\partial}{\partial\theta}\left(\frac{h}{r}\left(v+r\frac{\partial v}{\partial r}-\frac{\partial u}{\partial\theta}\right)\right), \tag{2.2}$$

$\boldsymbol{e}_\theta$:

$$\alpha^2\frac{\partial v}{\partial t}+u\frac{\partial v}{\partial r}+\frac{v}{r}\frac{\partial v}{\partial \theta}+\frac{uv}{r}+\frac{\sin\theta}{2h}w^2=-\frac{1}{r}\frac{\partial p}{\partial\theta}+\frac{1}{h}\frac{\partial}{\partial r}\left(\frac{h}{r}\left(v+r\frac{\partial v}{\partial r}-\frac{\partial u}{\partial\theta}\right)\right), \tag{2.3}$$

$\boldsymbol{e}_s$:

$$\begin{aligned}\alpha^2\frac{\partial w}{\partial t}+u\frac{\partial w}{\partial r}+\frac{v}{r}\frac{\partial w}{\partial\theta}+\frac{\delta w}{h}(u\cos\theta-v\sin\theta)&=\frac{D}{h}+\frac{\sqrt{2R_s}\alpha^3}{h}\cos t\\&+\frac{1}{r}\frac{\partial}{\partial\theta}\left(\frac{1}{hr}\left(h\frac{\partial w}{\partial\theta}-\delta r\sin\theta w\right)\right)-\frac{1}{r}\frac{\partial}{\partial r}\left(\frac{r}{h}\left(-h\frac{\partial w}{\partial r}-\delta\cos\theta w\right)\right),\end{aligned} \tag{2.4}$$

where $\alpha=(a^2/\nu T)^{1/2}$ is the Womersley parameter, and D and R_s are the Dean number and secondary streaming Reynolds number, which are defined as follows:

$$D=\sqrt{2\delta}\frac{P_0a^3}{\rho\nu^2},\quad R_s=\frac{\delta K^2T^3}{\nu\rho^2}. \tag{2.5a,b}$$

Note that in (2.5a), $P_0a^3/(\rho\nu^2)$ is also equal to $4Re$, where Re is the Reynolds number based on the maximum axial velocity of the flow that would be driven by the steady component of the pressure gradient in a straight pipe of radius a. The function $h(r,\theta)$ is given by $1+\delta r\cos\theta$, and $h(r,\theta)\,\Delta s$ is the distance travelled along the pipe by a particle with fixed r and θ as s increases by Δs. Equations (2.1)–(2.4) must be solved subject to the no-slip boundary condition $\boldsymbol{u}=\boldsymbol{0}$ at $r=1$.

It is convenient to introduce a streamfunction ψ via

$$u=\frac{1}{hr}\frac{\partial(h\psi)}{\partial\theta},\quad v=-\frac{1}{h}\frac{\partial(h\psi)}{\partial r}, \tag{2.6}$$

so that (2.1) is solved automatically. Eliminating the pressure from (2.2) and (2.3), we obtain the following equation

$$\alpha^2\frac{\partial(\mathscr{L}\psi)}{\partial t}+\frac{1}{r}\mathscr{J}\left(\frac{\mathscr{L}\psi}{h},h\psi\right)-\frac{w}{h}\mathscr{H}w=\mathscr{L}^2\psi, \tag{2.7}$$

where

$$\left.\begin{aligned} \mathscr{L}f &= \frac{1}{r}\frac{\partial}{\partial r}\left(\frac{r}{h}\frac{\partial(hf)}{\partial r}\right)+\frac{1}{r^2}\frac{\partial}{\partial\theta}\left(\frac{1}{h}\frac{\partial(hf)}{\partial\theta}\right), \\ \mathscr{J}(f,g) &= \frac{\partial f}{\partial r}\frac{\partial g}{\partial\theta}-\frac{\partial f}{\partial\theta}\frac{\partial g}{\partial r}, \quad \mathscr{H}f=\sin\theta\frac{\partial f}{\partial r}+\frac{\cos\theta}{r}\frac{\partial f}{\partial\theta}. \end{aligned}\right\} \tag{2.8}$$

The term $-h^{-1}w\mathscr{H}w$ in (2.7) represents the centrifugal force term arising from the curvature. The axial momentum equation (2.4) becomes

$$\alpha^2\frac{\partial w}{\partial t}+\frac{1}{hr}\mathscr{J}(w,h\psi)+\frac{\delta w}{h}\mathscr{H}\psi=\frac{D}{h}+\frac{\sqrt{2R_s}\alpha^3}{h}\cos t+\mathscr{L}w. \tag{2.9}$$

The term $h^{-1}\delta w\mathscr{H}\psi$ represents an inertial term due to the curvature of the pipe; it may be shown that this correction term is half the usual Coriolis force (Siggers & Waters 2005).

The governing equations are now (2.7) and (2.9), together with no-slip boundary conditions, $\psi=\psi_r=w=0$, at the outer boundary ($r=1$). Note that in the limit $\delta\to 0$, the third term in (2.9) disappears, while the centrifugal force term in (2.7) is retained. By considering finite values of δ, we will determine the effects of both the centrifugal and Coriolis forces on the flow.

One of the main goals will be to calculate the axial and azimuthal WSS (denoted τ_s and τ_θ, respectively). These are defined as

$$\tau_s=-\frac{1}{\sqrt{2\delta}}\frac{\partial w}{\partial r}\bigg|_{r=1}, \qquad \tau_\theta=-\frac{\partial v}{\partial r}\bigg|_{r=1}=\frac{\partial^2\psi}{\partial r^2}\bigg|_{r=1}, \tag{2.10}$$

respectively. To obtain the dimensional WSS, the above expressions must be multiplied by $\mu v/a^2$. It will also be useful to define the axial component of vorticity, which is given by

$$\xi=-\frac{1}{r}\frac{\partial u}{\partial\theta}-\frac{1}{r}\frac{\partial(rv)}{\partial r}=-\mathscr{L}\psi=-\frac{1}{r}\frac{\partial}{\partial r}\left(\frac{r}{h}\frac{\partial}{\partial r}(h\psi)\right)-\frac{1}{r^2}\frac{\partial}{\partial\theta}\left(\frac{1}{h}\frac{\partial}{\partial\theta}(h\psi)\right). \tag{2.11}$$

3. Oscillatory pressure gradient – asymptotic solution

Here we develop an asymptotic solution for (2.7) and (2.9) in the small-curvature regime, i.e. $\delta\ll 1$. We expand $w=\sum_{n=0}^{\infty}\delta^n w_n$, $\psi=\sum_{n=0}^{\infty}\delta^n\psi_n$, and the leading-order equations are

$$\alpha^2\frac{\partial\nabla^2\psi_0}{\partial t}+\frac{1}{r}\mathscr{J}(\nabla^2\psi_0,\psi_0)-w_0\mathscr{H}w_0=\nabla^4\psi_0, \tag{3.1}$$

$$\alpha^2\frac{\partial w_0}{\partial t}+\frac{1}{r}\mathscr{J}(w_0,\psi_0)=F+\nabla^2 w_0, \tag{3.2}$$

where $F(t)=D+\sqrt{2R_s}\alpha^3\cos t$ is the forcing term and ∇^2 is the usual two-dimensional Laplacian in polar coordinates. We proceed to solve these equations in the limit $|F(t)|\ll 1$ and $\alpha\ll 1$.

Inspection of (3.1) and (3.2) reveals that a consistent balance is obtained when w_0 is $O(F)$ and ψ_0 is $O(F^2)$. Writing $w_0=Fw_{00}+w_0'$ and $\psi_0=F^2\psi_{00}+\psi_0'$, where $|w_0'|\ll|Fw_{00}|$ and $|\psi_0'|\ll|F^2\psi_{00}|$, equation (3.2) yields a balance between the driving pressure gradient and the viscous terms, i.e. $0=1+\nabla^2 w_{00}$, whilst in (3.1), the centrifugal term drives the flow through the viscous term, i.e. $-w_{00}\mathscr{H}w_{00}=\nabla^4\psi_{00}$. These equations

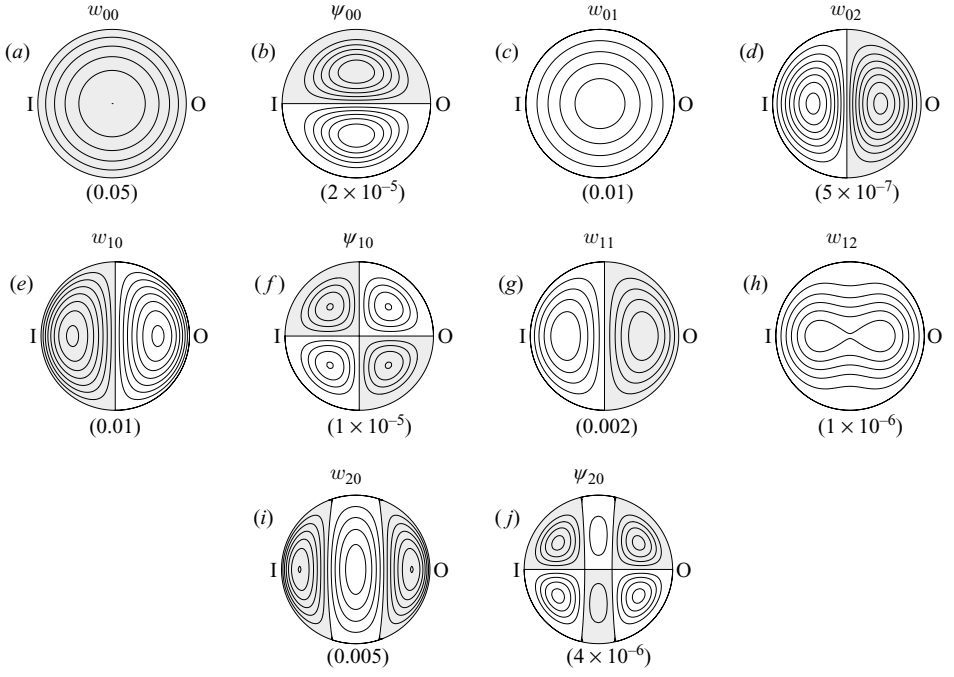

FIGURE 2. Contour plots of components of w and ψ. (a) represents the Poiseuille flow solution for a straight pipe and (b) represents the leading contribution to ψ. (c), (d), (g) and (h) show the corrections to w due to inertial effects; (c) and (g) arise from the time-dependent inertia term, whilst (d) and (h) come from the nonlinear inertial terms. (e) and (i) show the finite-curvature corrections to the axial velocity arising from balancing the viscous term with the pressure gradient. (f) and (j) show the correction to the streamfunction arising from the curvature. Shaded areas indicate regions where the function is positive, 'I' denotes the inside of the pipe bend ($\theta=\pi$) and 'O' denotes the outside ($\theta=0$), and the contour spacings are given underneath the figures in parentheses.

must be solved subject to the usual no-slip boundary conditions on the tube wall. The solutions are

$$w_{00}=\tfrac{1}{4}(1-r^2),\quad \psi_{00}=\frac{1}{2^{10}\times3^2}r(1-r^2)^2(4-r^2)\sin\theta.$$

Contour plots of w_{00} and ψ_{00} are shown in figures 2(a) and 2(b). Note that in all the cross-sectional figures in this paper 'I' denotes the inside of the pipe bend ($\theta=\pi$), 'O' denotes the outside ($\theta=0$) and shaded areas indicate regions where the function is positive. Contours are plotted at multiples of the numbers in parentheses underneath the figures. For the axial velocity plots, the zero contour corresponds to the boundary, and in the streamfunction and vorticity plots, the zero contour marks the separation between positive value (shading) and negative value (no shading) contours. The leading-order axial flow is the Poiseuille flow that would be obtained in a straight pipe, whilst the leading-order secondary flow is symmetric and consists of two Dean vortices, with flow from the inside of the bend to the outside, and back around the walls, agreeing with both the classical Dean flow and Mullin & Greated's observations (Dean 1928; Mullin & Greated 1980).

We now consider the corrections to the $O(\delta^0)$ solutions above arising from the inertial terms. Substituting $w_0 = Fw_{00} + w_0'$, $\psi_0 = F^2\psi_{00} + \psi_0'$ into (3.2), we obtain

$$\nabla^2 w_0' = \alpha^2 \frac{\mathrm{d}F}{\mathrm{d}t} w_{00} + \frac{F^3}{r}\mathscr{J}(w_{00}, \psi_{00}) + \cdots. \tag{3.3}$$

The two terms on the right-hand side of (3.3) are of order $\alpha^2 \mathrm{d}F/\mathrm{d}t$ and F^3, respectively. Thus, depending on the relative sizes of D, R_s and α, there are three possibilities for the size of w_0'.

(i) If $R_s^{1/2}\alpha^5 \gg \max(D^3, R_s^{3/2}\alpha^9)$, then the right-hand side of (3.3) is dominated by the first term. Writing the next correction to w_0 as $\alpha^2(\mathrm{d}F/\mathrm{d}t)w_{01}$, w_{01} is given by the solution of $\nabla^2 w_{01} = w_{00}$, which is

$$w_{01} = -\tfrac{1}{64}(1 - r^2)(3 - r^2).$$

(ii) If $R_s^{1/2}\alpha^5 \ll \max(D^3, R_s^{3/2}\alpha^9)$ then the right-hand side of (3.3) is dominated by the second term, and the next correction to w_0 is $F^3 w_{02}$, given by the solution of $\nabla^2 w_{02} = r^{-1}\mathscr{J}(w_{00}, \psi_{00})$, which is

$$w_{02} = \frac{1}{2^{15} \times 3^2 \times 5} r(1 - r^2)(19 - 21r^2 + 9r^4 - r^6)\cos\theta.$$

(iii) If $R_s^{1/2}\alpha^5 \sim \max(D^3, R_s^{3/2}\alpha^9)$, then both terms contribute at leading order to the right-hand side of (3.3) and so the next correction to w_0 is equal to $\alpha^2(\mathrm{d}F/\mathrm{d}t)w_{01} + F^3 w_{02}$.

Diagrams of w_{01} and w_{02} are given in figures 2(*c*) and 2(*d*), respectively. The spatially-symmetric term, w_{01}, is driven by the time-dependent inertia term, and leads to contributions to the axial velocity that lag behind the oscillations of w_{00} by $\pi/2$. The asymmetric term w_{02} is driven by the nonlinear inertial terms, and gives contributions that attain their maximum values at the same times as w_{00}; an additional effect of this term is to move the position where the maximal axial velocity is attained towards the outside of the bend.

We now consider equations (2.7) and (2.9) at $O(\delta)$:

$$\begin{aligned}\alpha^2 \frac{\partial \nabla^2 \psi_1}{\partial t} + \alpha^2 \frac{\partial \mathscr{L}_1 \psi_0}{\partial t} + \frac{1}{r}\mathscr{J}(\nabla^2\psi_1 + \mathscr{L}_1\psi_0 - r\cos\theta\nabla^2\psi_0, \psi_0) \\ + \frac{1}{r}\mathscr{J}(\nabla^2\psi_0, \psi_1 + r\cos\theta\psi_0) - (w_1 - r\cos\theta w_0)\mathscr{H}w_0 - w_0\mathscr{H}w_1 \\ = \nabla^4\psi_1 + \nabla^2\mathscr{L}_1\psi_0 + \mathscr{L}_1\nabla^2\psi_0,\end{aligned} \tag{3.4}$$

$$\begin{aligned}\alpha^2 \frac{\partial w_1}{\partial t} + \frac{1}{r}\mathscr{J}(w_1, \psi_0) + \frac{1}{r}\mathscr{J}(w_0, \psi_1 + r\cos\theta\psi_0) - \cos\theta\mathscr{J}(w_0, \psi_0) \\ + w_0\mathscr{H}\psi_0 = -r\cos\theta F + \nabla^2 w_1 + \mathscr{L}_1 w_0,\end{aligned} \tag{3.5}$$

where $\mathscr{L}_1$ is the $O(\delta)$-component of $\mathscr{L}$, given by

$$\mathscr{L}_1 f = \frac{\cos\theta}{r}\frac{\partial(rf)}{\partial r} - \frac{1}{r}\frac{\partial(f\sin\theta)}{\partial\theta}.$$

As before, writing $w_1 = Fw_{10} + w_1'$, $\psi_1 = F^2\psi_{10} + \psi_1'$, where $|w_1'| \ll |Fw_{10}|$ and $|\psi_1'| \ll |F^2\psi_{10}|$, equations (3.4) and (3.5) yield at leading order

$$\begin{aligned}\nabla^4\psi_{10} &= -(w_{10} - rw_{00}\cos\theta)\mathscr{H}w_{00} - w_{00}\mathscr{H}w_{10} - \nabla^2\mathscr{L}_1\psi_{00} - \mathscr{L}_1\nabla^2\psi_{00}, \\ \nabla^2 w_{10} &= rF\cos\theta - \mathscr{L}_1 w_{00},\end{aligned}$$

which have solutions

$$w_{10} = -\tfrac{3}{16} r(1-r^2)\cos\theta, \tag{3.6}$$

$$\psi_{10} = -\frac{1}{2^{12}\times 3^2\times 5} r^2(1-r^2)^2(56-17r^2)\sin 2\theta. \tag{3.7}$$

These are shown in figures 2(*e*) and 2(*f*) respectively. Inspecting figure 2(*e*), we see that as the curvature is increased, the point where the maximal axial velocity is attained moves towards the inside of the pipe bend. This reduces the asymmetry induced by the term $F^3 w_{02}$ (thus to this order, the degree of asymmetry in the axial velocity profile depends on the relative sizes of the terms $F^3 w_{02}$ and $\delta F w_{10}$). From figure 2(*f*), the effect of ψ_{10} is to move the centre of the Dean vortices towards the inside of the bend (see also Siggers & Waters 2005).

As at $O(\delta^0)$, the three cases (i), (ii) and (iii) apply, depending on the relative sizes of D, R_s and α.

(i) w_1' is dominated by $\alpha^2(\mathrm{d}F/\mathrm{d}t)w_{11}$, which satisfies

$$w_{10} = \nabla^2 w_{11} + \mathscr{L}_1 w_{01},$$

and has solution

$$w_{11} = \frac{1}{2^7\times 3} r(1-r^2)(11-4r^2)\cos\theta,$$

shown in figure 2(*g*).

(ii) w_1' is dominated by $F^3 w_{12}$, where

$$\frac{1}{r}\mathscr{J}(w_{10},\psi_{00}) + \frac{1}{r}(w_{00},\psi_{10}+r\psi_{00}\cos\theta) - \mathscr{J}(w_{00},\psi_{00})\cos\theta + w_{00}\mathscr{H}\psi_{00} = \nabla^2 w_{12} + \mathscr{L}_1 w_{02},$$

which has solution

$$w_{12} = \frac{1}{2^{18}\times 5^2\times 3^3}(1-r^2)(-6(148+43r^2-132r^4+68r^6-7r^8) - 5r^2(463-613r^2+296r^4-40r^6)\cos 2\theta),$$

shown in figure 2(*h*).

(iii) w_1' has contributions of the same order from both $\alpha^2(\mathrm{d}F/\mathrm{d}t)w_{11}$ and $F^3 w_{12}$.

From the equations at $O(\delta^2)$, we may work out series expansions for w_2 and ψ_2 in a similar way, finding that $w_2 = F w_{20} + w_2'$ and $\psi_2 = F^2\psi_{20} + \psi_2'$, where $|w_2'| \ll |w_{20}|$ and $|\psi_2'| \ll |\psi_{20}|$, and

$$w_{20} = \frac{1}{128}(1-r^2)(-3+11r^2+10r^2\cos 2\theta),$$

$$\psi_{20} = \frac{1}{2^{17}\times 3^2\times 5} r(1-r^2)^2(-(133-976r^2+327r^4)\sin\theta + 2r^2(499-172r^2)\sin 3\theta).$$

Plots of w_{20} and ψ_{20} are shown in figures 2(*i*) and 2(*j*).

Thus we have shown that

$$w = \left[F w_{00} + \alpha^2\frac{\mathrm{dF}}{\mathrm{d}t}w_{01} + F^3 w_{02} + O\left(\alpha^4\frac{\mathrm{d}^2F}{\mathrm{d}t^2}, F^5\right)\right] + \delta\left[F w_{10} + \alpha^2\frac{\mathrm{d}F}{\mathrm{d}t}w_{11} + F^3 w_{12} + O\left(\alpha^4\frac{\mathrm{d}^2\mathrm{F}}{\mathrm{d}t^2}, F^5\right)\right] + \delta^2\left[F w_{20} + O\left(\alpha^2\frac{\mathrm{d}F}{\mathrm{d}t}, F^3\right)\right] + O(\delta^3), \tag{3.8}$$

and an analogous expression may be written for the streamfunction. Details of the terms that may be retained and their ordering depends on the relative sizes of the small quantities δ, α and F. For the sake of brevity we omit a full presentation of the different cases here.

The total dimensionless axial flow rate through the pipe is equal to

$$\int_0^{2\pi}\int_0^1 rw\,\mathrm{d}r\,\mathrm{d}\theta = 2\pi\left(\left(\frac{F}{16}-\frac{\alpha^2}{96}\frac{\mathrm{d}F}{\mathrm{d}t}+\cdots\right)+\delta\left(-\frac{11F^3}{2^{16}\times 3^3\times 5}+\cdots\right)+\delta^2\left(\frac{F}{2^8\times 3}+\cdots\right)+O(\delta^3)\right), \quad (3.9)$$

where the $\cdots$ refer to higher-order terms in the expansions, and the time-averaged axial flow rate is

$$2\pi D\left(\left(\frac{1}{16}+\cdots\right)+\delta\left(-\frac{11(D^2+3R_s\alpha^6)}{2^{16}\times 3^3\times 5}+\cdots\right)+\delta^2\left(\frac{1}{2^8\times 3}+\cdots\right)+O(\delta^3)\right). \quad (3.10)$$

Thus, as δ increases from zero, the time-averaged axial flow rate decreases, reaching a minimum as δ approaches $11(D^2+3R_s\alpha^6)/(2^9\times 5\times 3^2)$.

The maximum axial velocity is

$$\left(\frac{F}{4}-\frac{3\alpha^2}{64}\frac{\mathrm{d}F}{\mathrm{d}t}+\cdots\right)+\delta\left(-\frac{581F^3}{2^{18}\times 3^2\times 5^2}+\cdots\right)+\delta^2\left(\frac{3F}{256}+\cdots\right)+O(\delta^3), \quad (3.11)$$

which is attained at the point

$$r=|\bar{r}|\ ,\ \theta=\begin{cases}0+\cdots & \text{if } \bar{r}\geqslant 0,\\ \pi+\cdots & \text{if } \bar{r}<0,\end{cases} \quad \text{where } \bar{r}=\left(\frac{19F^2}{2^{14}\times 3^2\times 5}+\cdots\right)+\delta\left(-\frac{3}{8}-\frac{7\alpha^2}{192}\frac{1}{F}\frac{\mathrm{d}F}{\mathrm{d}t}+\cdots\right)+O(\delta^2), \quad (3.12)$$

where, owing to symmetry, for many parameter regimes the maximum is attained exactly on the centreline $\theta=0,\pi$. As mentioned earlier, w_{10} and w_{02} move the position of this maximum in opposite directions. For $F^2\gg\delta$, the term containing w_{02} dominates that containing w_{10}, so the maximum is located towards the outside of the bend; as δ increases, the maximum moves towards the inside. The maximum of the streamfunction is

$$[(1.18\times 10^{-4}F^2+\cdots)+\delta(\cdots)+\delta^2(1.43\times 10^{-5}F^2+\cdots))]+O(\delta^3), \quad (3.13)$$

which is attained at the vortex centre

$$r=(0.43+\cdots)+\delta(\cdots)+\delta^2(0.06+\cdots)+O(\delta^3), \quad (3.14)$$

$$\theta=(\pi/2+\cdots)+\delta(0.59+\cdots)+O(\delta^2), \quad (3.15)$$

where the numerical coefficients here have been expressed to two decimal places. This indicates that the secondary-flow vortices also move towards the inside of the bend of the pipe as δ increases.

The axial WSS is given by

$$\tau_s=\frac{1}{\sqrt{2\delta}}\left(\frac{F}{2}-\frac{\alpha^2}{16}\frac{\mathrm{d}F}{\mathrm{d}t}+\frac{F^3\cos\theta}{2^{13}\times 5\times 3}+\cdots\right)+\frac{\sqrt{\delta}}{\sqrt{2}}\left(-\frac{3F\cos\theta}{8}+\frac{7\alpha^2\cos\theta}{192}\frac{\mathrm{d}F}{\mathrm{d}t}-\frac{F^3(72+53\cos 2\theta)}{2^{16}\times 5\times 3^3}+\cdots\right)+\frac{\delta^{3/2}}{\sqrt{2}}\left(\frac{F(4+5\cos 2\theta)}{32}+\cdots\right)+O(\delta^{5/2}). \quad (3.16)$$

For $\delta\ll(D^2+3R_s\alpha^6)/(2^{10}\times 5\times 3^2)$, the time-averaged value of τ_s has maximum and minimum values of

$$\frac{D}{2\sqrt{2\delta}}\left(1 \pm \frac{D^2 + 3R_s\alpha^6}{2^{12} \times 5 \times 3} + \cdots\right) + \frac{\sqrt{\delta}}{\sqrt{2}} D\left(\mp\frac{3}{8} - \frac{25(D^2 + 3R_s\alpha^6)}{2^{16} \times 3^3} + \cdots\right) + \frac{\delta^{3/2}}{\sqrt{2}} D\left(\frac{9}{2^5} + \cdots\right) + O(\delta^{5/2}), \quad (3.17)$$

attained at $\theta = 0$ and $\theta = \pi$, respectively. The maximum value of the azimuthal WSS is attained at

$$\theta = \left(\frac{\pi}{2} + \cdots\right) + \delta\left(\frac{13}{10} + \cdots\right) + O(\delta^2), \quad (3.18)$$

and is equal to

$$\left(\frac{1}{384}F^2 + \cdots\right) + \delta(\cdots) + \delta^2\left(\frac{1237}{2^{13} \times 3 \times 5^2}F^2 + \cdots\right) + O(\delta^3). \quad (3.19)$$

Finally, considering the accuracy of our series solution, we know from Dean (1928) that when $R_s = 0$ these results should be reasonably accurate for $D \lesssim 100$. However, the corresponding limiting values for δ, α and R_s are not as well known, and we shall investigate the accuracy of these analytical results in later sections by comparison with the numerical solutions.

4. Sinusoidal pressure gradient

We now consider flows driven by a sinusoidal (zero mean) pressure gradient. The governing equations are given by (2.7) and (2.9) with D set to zero.

4.1. *Numerical method*

Since accurate determination of the time dependent solution is required, the time stepping is done using the second-order backwards difference formula, which has error $O(\mathrm{d}t^2)$ where $\mathrm{d}t = 2\pi/N$ is the time step, and N is the number of time steps per period. This approximates time derivatives at the $(n+1)$th step by an expression involving the quantity at the $(n-1)$th, nth and $(n+1)$th steps. For simplicity, we replace the nonlinear terms from (2.7) and (2.9) at the $(n+1)$th step by a combination of their values at the nth and $(n-1)$th steps that has error $O(\mathrm{d}t^2)$. Thus (2.7) and (2.9) may then be approximated by

$$\mathscr{A}_1\psi^{n+1} = b_1, \quad \mathscr{A}_2 w^{n+1} = b_2, \quad (4.1)$$

where ψ^{n+1} and w^{n+1} denote solutions at the $(n+1)$th step, $\mathscr{A}_1$ and $\mathscr{A}_2$ are constant linear differential spatial operators and b_1 and b_2 are nonlinear functions of ψ^n, ψ^{n-1}, w^n, w^{n-1} and their spatial derivatives.

Equations (4.1) are discretized spatially using a pseudospectral method in the azimuthal direction and second-order central differencing in the radial direction. The resulting algebraic equations are solved using the HSL sparse matrix routine MA38.† The radial grid is defined by $r_0 = 0 < r_1 < r_2 < \cdots < r_{n_r-1} < r_{n_r} = 1$ and azimuthal discretization is performed by approximating functions of θ as $f(\theta) = \sum_{j=-n_\theta}^{n_\theta} f_j \mathrm{e}^{\mathrm{i}j\theta}$, where n_θ is some chosen truncation level, $f_0 \in \mathbb{R}$ and $f_j = \overline{f_{-j}} \in \mathbb{C}$ for $j \neq 0$, where overlines represent complex conjugates. The numerical approximations to $\psi(r_k, \theta, n\,\mathrm{d}t)$ and $w(r_k, \theta, n\,\mathrm{d}t)$ at $r = r_k$ and θ are denoted by $\sum_j \psi_{kj}^n \mathrm{e}^{\mathrm{i}j\theta}$ and $\sum_j w_{kj}^n \mathrm{e}^{\mathrm{i}j\theta}$, respectively. From the solution for ψ we can also evaluate the numerical approximation to the axial vorticity, $\xi(r_k, \theta, n\mathrm{d}t)$, at $r = r_k$ and θ, which is denoted $\sum_j \xi_{kj}^n \mathrm{e}^{\mathrm{i}j\theta}$.

† Obtainable from http://www.cse.clrc.ac.uk/nag/hsl/.

The boundary layers are resolved by using a finer mesh in areas with steep gradients in the variables. Care must be taken when evaluating derivatives at the pipe wall and at the origin. To take finite differences of the variables at $r = r_{n_r-1}$, it is necessary to introduce a fictitious grid point that lies outside the circular domain at $r_{n_r+1} = 2 - r_{n_r-1}$, and near the origin we introduce fictitious radial grid points at $r_{-1} = -r_1$ and $r_{-2} = -r_2$. For more details see Siggers & Waters (2005).

In the following section we identify two types of time-dependent behaviour: periodic with period $2k\pi$, $k \in \mathbb{N}$; and quasi-periodic. We test for convergence to a time-periodic solution with period 2π after m periods of simulation by requiring that the conditions

$$\max_{(k,j)\in S_1} \left| \frac{\xi_{kj}^{mN} - \xi_{kj}^{(m-1)N}}{\xi_{kj}^{(m-1)N}} \right| < \mathrm{err}_1, \quad \max_{(k,j)\in S_2} \left| \frac{w_{kj}^{mN} - w_{kj}^{(m-1)N}}{w_{kj}^{(m-1)N}} \right| < \mathrm{err}_2,$$

hold, where the err_i are chosen small positive constants and

$$S_1 = \{(k, j) : 0 \leqslant k < n_r,\ 0 \leqslant j \leqslant n_\theta,\ |\xi_{kj}^{n-1}| > \epsilon_1\},$$
$$S_2 = \{(k, j) : 0 \leqslant k < n_r,\ 0 \leqslant j \leqslant n_\theta,\ |w_{kj}^{n-1}| > \epsilon_2\},$$

for chosen small constants ϵ_1 and ϵ_2. For $2k\pi$ periodic solutions, we compare solutions with time differences of $2k\pi$ in the analogous manner. For quasi-periodic solutions, we cannot determine convergence in this manner; however, we simulate the solution for at least ten times the normal time for convergence, and we infer the quasi-periodicity of the solutions from the bifurcation structure (see § 4.2.1).

The simulations were run using 110 mesh points in the radial direction: these were spaced at intervals of 0.01 for $0 < r < 0.9$, and at intervals of 0.005 in the boundary-layer region corresponding to $0.9 < r < 1$. We used 21 modes in the azimuthal direction. We tested the accuracy by refining the radial mesh, increasing the number of azimuthal modes and reducing the tolerance criteria. The code was also validated by comparison of the numerical results with the asymptotic solutions found in § 3; see § 6.

4.2. *Results*

4.2.1. *Bifurcation structure*

All the solutions found in § 3 were both 2π-periodic and spatially symmetric in the centreplane ($\theta = 0, \pi$). In addition, the solution was unique. In our numerical results with small and moderate values of R_s and α we also find 2π-periodic and symmetric solutions, as expected. However, in other regions of parameter space, our numerical results reveal parameter values where there are multiple solutions to the governing equations. With α and δ fixed at 10 and 0.1, respectively, a sketch of the proposed bifurcation structure consistent with the observations as R_s is varied is given in figure 3. The vertical axis (not to scale) denotes the value of a solution property on a Poincaré section at time intervals of 2π, e.g. values of the maximum axial velocity at $t = 2\pi k$ where $k \in \mathbb{N}$. In the following discussion the term *symmetric* is used to refer to solutions that are spatially symmetric in the centreplane ($\theta = 0, \pi$). We have identified three distinct classes of stable solution: periodic and symmetric (branch 1, see e.g. figure 6), periodic and asymmetric (branch 2, see e.g. figure 8), and solutions that are asymmetric and also either quasi-periodic, or periodic but having a period $2\pi k$ for $k \in \mathbb{N}$ (branch 3). Since branch 3 solutions are not in general 2π periodic, the solution takes a range of values on the vertical axis in figure 3, as indicated by the dotted ellipse: the upper and lower curves emerging from (B) are both part of the same solution, and represent the envelope of the solutions. In figure 3, we use solid curves to denote stable solutions and dashed curves to denote unstable solutions;

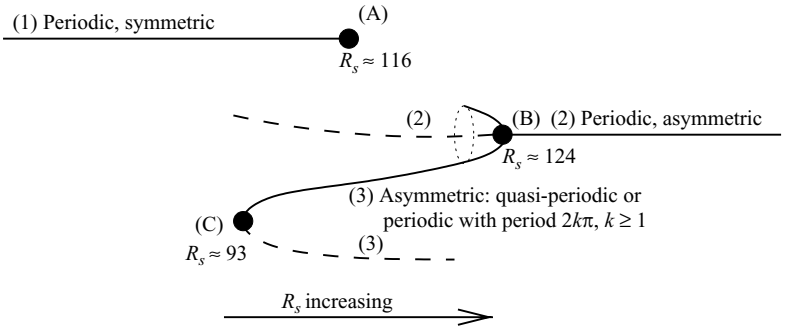

FIGURE 3. Sketch of proposed bifurcation diagram for $\alpha = 10$ and $\delta = 0.1$, showing the existence of multiple branches of solutions. The vertical axis (not to scale) denotes the value (or range of values) of a solution property on a Poincaré section at time intervals of 2π. Solid curves: stable solutions; dashed curves: unstable solutions. Branch 3 solutions are not in general 2π-periodic, and the solution takes a range of values on the vertical axis, as indicated by the dotted ellipse.

note that we are only able to find stable solutions with our numerical scheme, and we infer the presence of unstable branches from our observations as R_s varies. We obtain branch 1 solutions by solving the governing equations at a given (small) R_s using the asymptotic solution obtained in § 3 as an initial condition. Increasing R_s gradually, we can proceed along branch 1 to bifurcation point (A). Upon increasing R_s further, we obtain solutions on either branch 3 or branch 2 (depending on the value of R_s at which bifurcation (B) occurs). If, for example, we move onto branch 3 initially, we can obtain branch 2 solutions by further increasing R_s to travel through bifurcation (B). Alternatively, if we obtain a branch 2 solution, we can find branch 3 solutions via a decrease in R_s.

At point (A), the branch 1 solutions lose stability via a bifurcation, as shown in figure 3. From the numerical results, the transition is discontinuous and hysteretic, meaning that (A) could be a subcritical pitchfork bifurcation (producing two unstable branches related by a centreplane reflection), a saddle-node bifurcation (in which branch 1 collides with an unstable branch of solutions and the two branches are annihilated), or a global bifurcation. An analysis of the bifurcation at (A) would require investigation of the behaviour of the eigenvalues on branch 1, and is beyond the scope of this paper. Starting from a stable branch 2 solution, if we decrease R_s, the solution will undergo a Hopf bifurcation (B) to produce a single branch of solutions (branch 3). Upon decreasing R_s further, the branch 3 solutions will lose stability via a saddle-node bifurcation (C), and a branch 1 solution will be seen.

The values of R_s at which bifurcations (A), (B), (C) occur as a function of the curvature, δ, are given in figure 4 (again for $\alpha = 10$). Bifurcation (C) always occurs at a lower value of R_s than (B), but when $\delta \lesssim 0.07$, (B) occurs at a lower value of R_s than (A). Thus if $\delta < 0.07$, then as R_s is increased, branch 1 solutions will undergo a transition to branch 2 solutions. Conversely, if $\delta \gtrsim 0.07$, the branch 1 solution will initially undergo a transition to a branch 3 solution when it loses stability, and will undergo a further transition to branch 2 solutions upon raising R_s further. Thus the transitions seen in the solution depend qualitatively upon the pipe curvature.

The frequency of the periodic branch 2 solutions is 1, whereas the frequency, ω, associated with the Hopf bifurcation (B) is expected to vary continuously along the curve (B) in figure 4. If $\omega = p/q$ is rational, then the branch 3 solution for R_s just

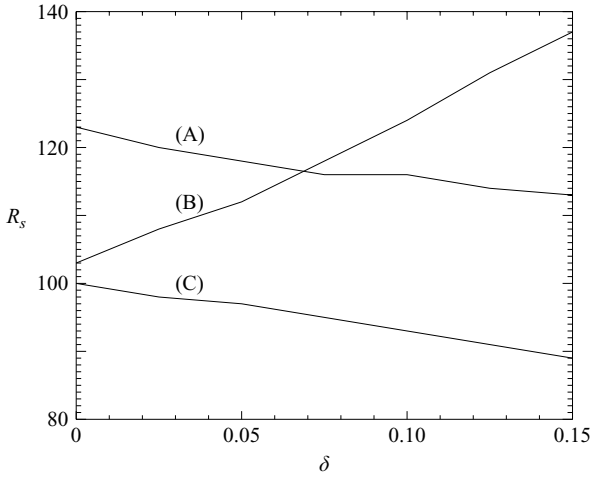

FIGURE 4. Plot of the critical secondary streaming Reynolds number, R_s, at which the bifurcations occur against δ. (B), Hopf; (C), saddle-node. Here, $\alpha = 10$.

below (B) will be periodic with period $2\pi q$; otherwise the branch 3 solution will be quasi-periodic there. Thus in the parameter space just below curve (B) in figure 4, we expect to see Arnol'd tongues and mode-locking (see Glendinning 1994 pp. 267–271). If we move through a path in parameter space that crosses the curve (B) transversely (e.g. keeping all parameters fixed except for R_s), then the solutions seen will typically pass through an infinite sequence of Arnol'd tongues each of which corresponds to a rational frequency p_i/q_i. The solution within the tongue is periodic, or mode locked, with period $2\pi q_i$; between the tongues, the solution is quasi-periodic.

We have not investigated the effect of α on the intersection of curves labelled (B) and (C) in figure 4. However, the behaviour illustrated for $\alpha = 10$ in figure 4, namely the curvature-dependent hysteresis to asymmetric solutions, and the finite 'window' of quasi-periodicity will persist, at least for values of α in a neighbourhood of $\alpha = 10$.

4.2.2. *Solutions at low and moderate values of* α

We now discuss features of the solutions in more detail. A typical branch 1 solution is illustrated in figure 5, which shows the streamlines and axial velocity profiles for $\delta = 0$, $R_s = 10$ and $\alpha = 10$. The solutions are presented at eight equally spaced times around the period. The top row of figures shows the secondary streamlines, and the bottom row the axial velocity at the corresponding times (black represents positive values and white represents negative values). During the first half-period, the direction of the secondary flow is anticlockwise in the top half of the circular domain and clockwise in the bottom half; the directions reverse in the second half-period. The symmetric solutions also possess a temporal symmetry in which the solution is translated forward by half a period and the sign of the axial velocity is reversed.

The dependence of branch 1 solutions on the curvature, δ, is shown in figure 6 for $R_s = 10$, $\alpha = 1$ and $\delta = 0, 0.1$ and 0.3. In figures 6, 8, 9, 11, 15–19, solid, dotted and dashed curves represent solutions with $\delta = 0, 0.1, 0.3$, respectively, and the shading indicates regions where the solution with $\delta = 0$ is positive, unless otherwise stated. The streamlines, axial velocity and axial vorticity contours are shown at equally spaced time points for the first half-period corresponding to $t = 0, \pi/3, 2\pi/3$. The qualitative features of the solution are captured by the $\delta = 0$ solution, and both the centre of the

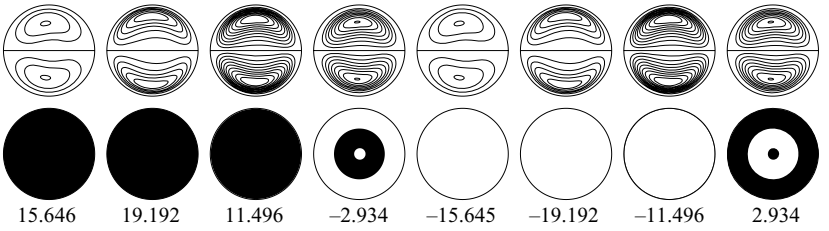

FIGURE 5. Streamlines and axial velocity plots for $\delta = 0$, $R_s = 10$ and $\alpha = 10$. The top row shows the streamlines in the cross-section at eight equally spaced times around the period ($t = k\pi/4$, $k = 1, 2, \ldots, 8$), whilst the second row shows the axial velocity at the corresponding times (black represents positive values and white represents negative values). The numbers underneath (which must be multiplied by 2π) give the total dimensionless axial flow rate (see (3.9)).

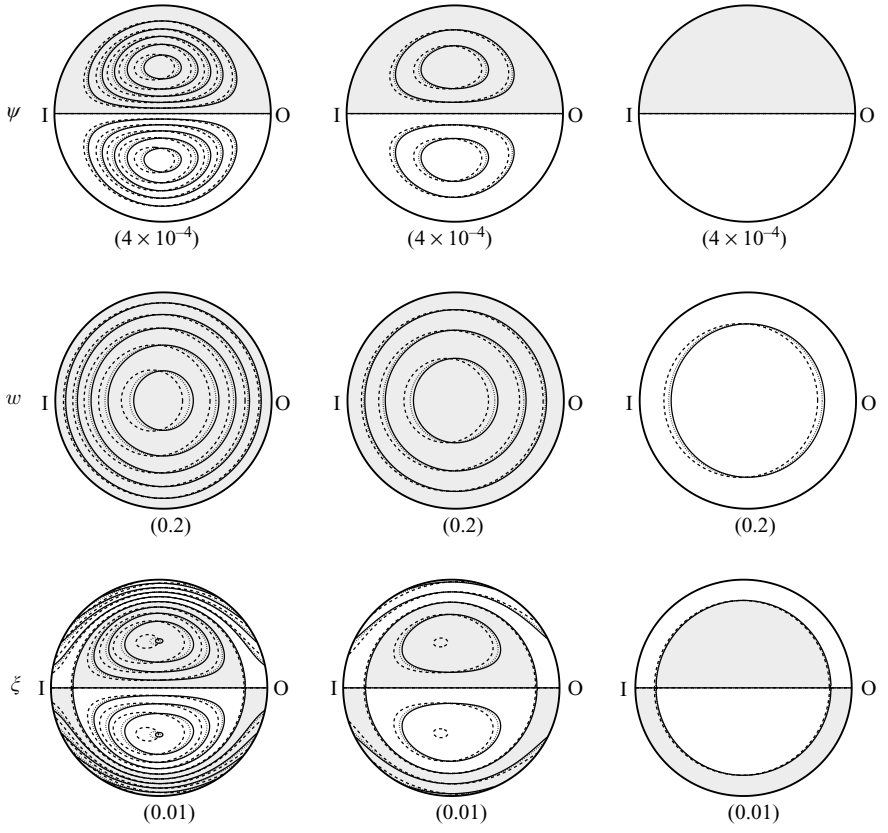

FIGURE 6. Streamlines, axial velocity contours and axial vorticity contours for $R_s = 10$ and $\alpha = 1$, each of which is shown at equally spaced time points for the first half-period ($t = 0, \pi/3, 2\pi/3$, respectively). Solid curves, $\delta = 0$; dotted curves, $\delta = 0.1$; dashed curves, $\delta = 0.3$. The shading indicates regions where the solution with $\delta = 0$ is positive. The figures in parentheses underneath the plots give the spacing of the contour lines, and 'I' denotes $\theta = \pi$ whilst 'O' denotes $\theta = 0$.

vortex in the streamlines and the position at which the maximum of the axial velocity occurs is advected towards the inside of the pipe bend as δ increases. Inspection of (3.8) shows that the behaviour as δ increases, namely that the position of the maximum moves towards the inside bend, can be explained in terms of the Fw_{10} term.

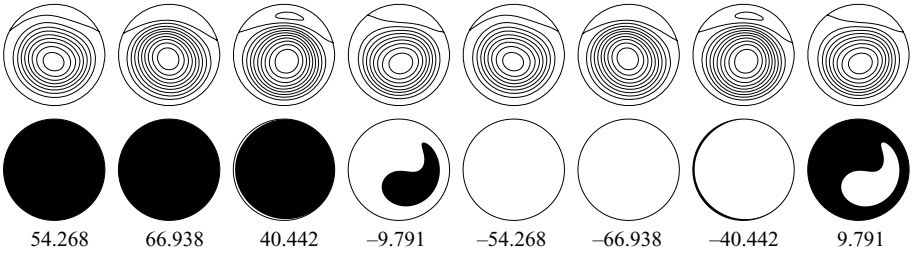

FIGURE 7. Streamlines and axial velocity plots for $\delta = 0$, $R_s = 120$ and $\alpha = 10$. The top row shows the streamlines in the cross-section at eight equally spaced times around the period ($t = k\pi/4$, $k = 1, 2, \ldots, 8$), whilst the second row shows the axial velocity at the corresponding times (black represents positive values and white represents negative values). The numbers underneath (which must be multiplied by 2π) give the total flow rate (the integral of the axial velocity).

Staying on branch 1, we see that, for larger values of R_s, the solution is qualitatively similar to the solution in figure 6. For $R_s = 300$ and $\alpha = 1$, for example, the maximum values of ψ and ξ increase by a factor of approximately 30, whilst the maximum of w increases by about $\sqrt{30}$ compared with the maximum values for $R_s = 10$ and $\alpha = 1$. This agrees with the predictions in § 3 that the axial velocity and streamfunction are dominated by Fw_{00} and $F^2\psi_{00}$, and are thus proportional to $\sqrt{R_s}$ and R_s, respectively.

We now return to the solution pictured in figure 5, and investigate what happens upon increasing R_s whilst keeping $\delta = 0$, $\alpha = 10$ fixed. Figure 4 indicates that for these values of α and δ, bifurcation (B) occurs at a lower value of R_s than (A). Thus as we increase R_s, the branch 1 solutions will lose stability to branch 2 solutions, such as that shown in figure 7. As we increase R_s further, the two vortices in the streamlines become more equal both in area and in terms of the maximum absolute values attained by the streamfunction in each vortex, i.e. the solution actually becomes closer to being symmetric. As mentioned previously, there are two sub-branches of branch 2, related via a reflection in the centreplane, and figures 7 and 8 show the solutions on the two different sub-branches. In the example shown in figure 8, the qualitative features of the solution are captured by the $\delta = 0$ solution.

Owing to their lack of 2π-periodicity, it is difficult to present a branch 3 solution compactly in a diagram; additionally, at any given time they resemble the branch 2 solutions with similar parameter values. However, if we plot a solution property (e.g. centreline axial velocity) against time, the quasi-periodic or multi-periodic nature of the solution is revealed, see for example figure 10, which shows the centreline velocity against time for several periods of the driving pressure gradient.

If instead we fix $R_s = 300$ and increase α from 1 to 10 (see figure 8), we also see a transition from a branch 1 to a branch 2 solution. This happens suddenly, suggesting that the transition is also discontinuous and hysteretic, and may therefore be a continuous deformation of bifurcation (A), i.e. starting from a branch 2 solution and reducing α, the value of α at which the branch 1 solution is seen is lower than the value of α at which the branch 1 solution loses stability as α is increased.

4.2.3. *Solutions at high values of* α

We now consider the solutions for higher values of α. In this case, the solutions we have found are all on branch 1. However, when α increases, it becomes increasingly difficult to resolve solutions with higher values of R_s, and therefore we cannot rule out the possible existence of asymmetric solution branches. At large values of α, we expect

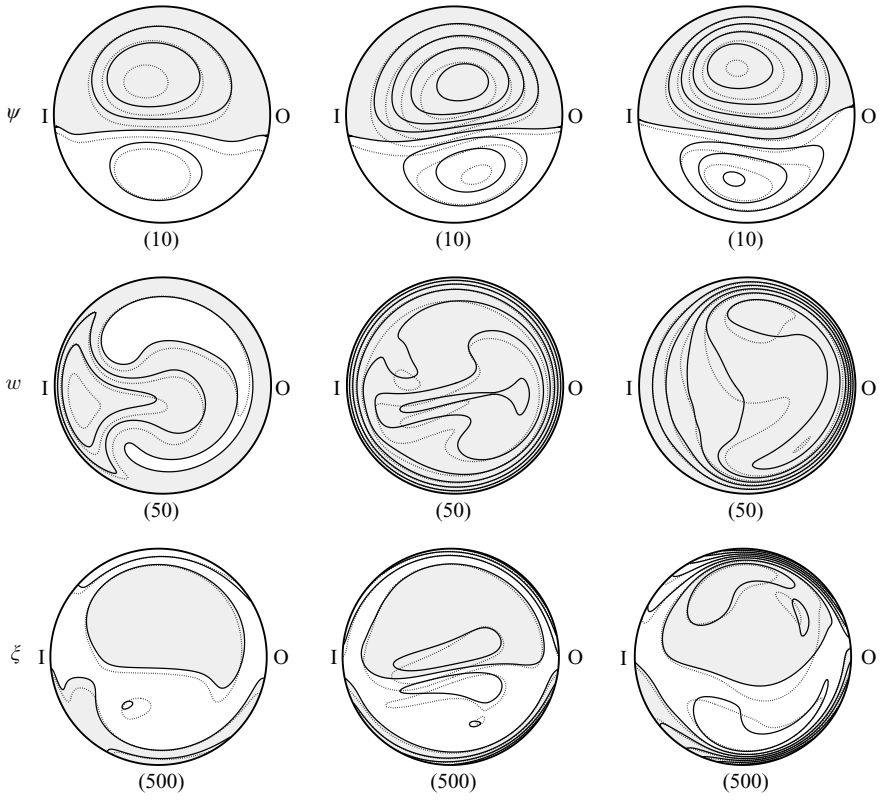

FIGURE 8. Streamlines, axial velocity contours and axial vorticity contours for $R_s = 300$, $\alpha = 10$ and $\delta = 0$ and 0.1, shown at $t = 0, \pi/3, 2\pi/3$. Solid curves, $\delta = 0$; dotted curves, $\delta = 0.1$.

the flow to consist of an inviscid core surrounded by a Stokes boundary layer (Stuart 1966; Lyne 1971). Figure 9 shows the solutions with $\alpha = 20$ and $R_s = 10$, and clearly shows the formation of a boundary layer at $r = 1$. The axial vorticity is almost constant in the core in all cases, whilst the axial velocity is approximately constant in the core for $\delta = 0$, whereas for $\delta = 0.3$ it is approximately independent of the vertical coordinate. For smaller α, the streamlines form two vortices filling the interior (e.g. at $\alpha = 1$, in figure 6), but in figure 9 where $\alpha = 20$ and $R_s = 10$, a second vortex pair has formed in the centre of the pipe. This second pair gradually expands as α increases until it occupies the whole interior of the pipe, with the original pair of vortices now confined to the boundary layer at $r = 1$. Figure 11 shows how the width of the boundary layer decreases with α, indicating that the width is proportional to α^{-1} for large α.

The presence of the boundary layer at large values of α makes the solution costly to find numerically. However, in the limit $\alpha \to \infty$, we can solve the boundary-layer equations analytically. The boundary-layer analysis provides a boundary condition on the core flow, which we will then solve using both analytical and numerical methods.

4.3. *Asymptotic analysis for high-frequency sinusoidal flow*

We now generalize the analysis of Stuart (1966) and Lyne (1971) to curved pipes with finite curvature. We expand the dependent variables in powers of α^{-1} as follows

$$\psi = \psi_0 + \alpha^{-1}\psi_1 + \alpha^{-2}\psi_2 + \cdots, \quad w = \alpha w_0 + w_1 + \alpha^{-1} w_2 + \cdots. \tag{4.2}$$

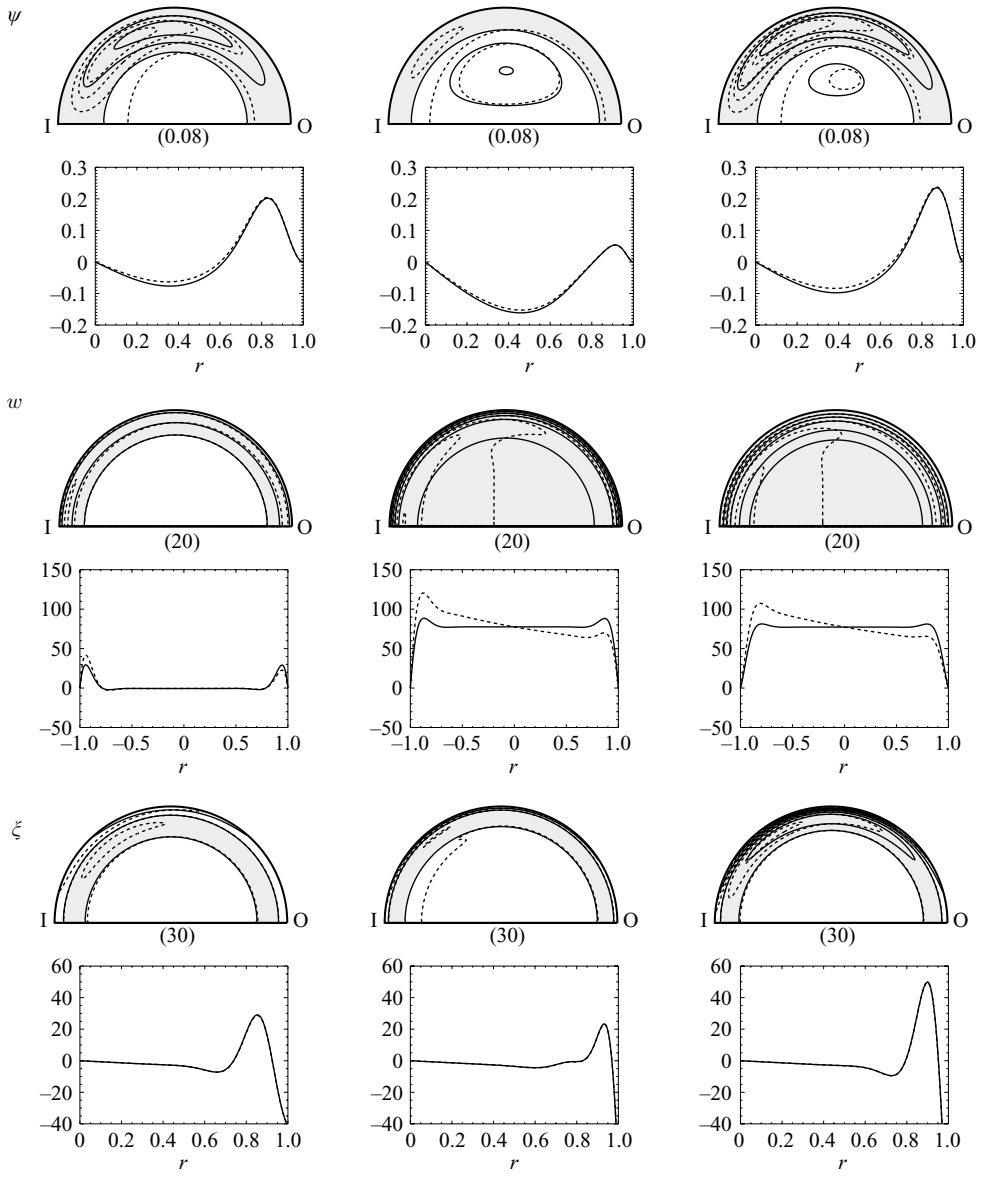

FIGURE 9. Streamlines, axial velocity contours and axial vorticity contours for $R_s = 10$ and $\alpha = 20$, shown at $t = 0, \pi/3, 2\pi/3$. The solutions are shown only for $\delta = 0$ and $\delta = 0.3$ for clarity and only half the cross-section is shown, since the solutions are symmetric. The graphs underneath the contour plots show the behaviour of the solutions on $\theta = \pi/2$ for ψ and ξ and on the horizontal diameter for w. Solid curves, $\delta = 0$; dashed curves, $\delta = 0.3$.

Assuming that $w|_{t=0} \equiv 0$, by considering successive orders of magnitude in (2.7) and (2.9), we obtain the following:

$$w_0 = \frac{1}{h}\sqrt{2R_s}\sin t, \quad w_1 = 0, \quad w_2 = 0, \tag{4.3}$$

$$\mathscr{L}\frac{\partial \psi_0}{\partial t} = 0, \quad \mathscr{L}\frac{\partial \psi_1}{\partial t} = 0, \quad \mathscr{L}\frac{\partial \psi_2}{\partial t} + \frac{1}{r}\mathscr{J}\left(\frac{\mathscr{L}\psi_0}{h}, h\psi_0\right) = \mathscr{L}^2\psi_0. \tag{4.4a–c}$$

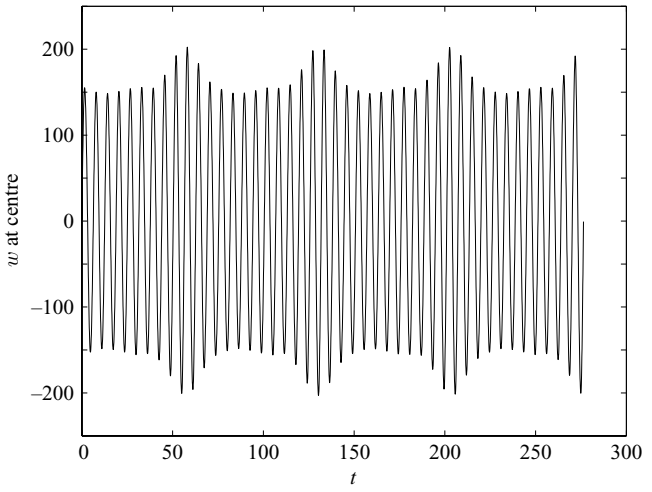

FIGURE 10. Plot of axial velocity at $r = 0$ as a function of time. Here, $\delta = 0.1$, $\alpha = 10$ and $R_s = 117$.

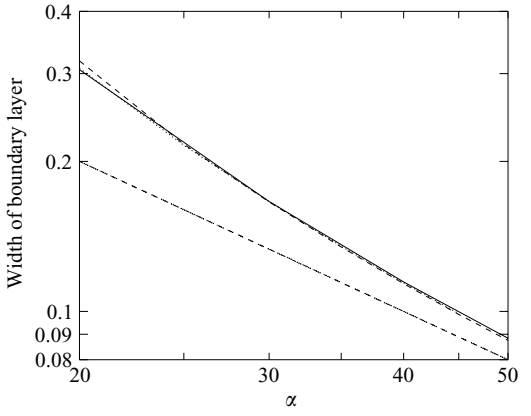

FIGURE 11. Logarithmic plot of width of boundary layer (averaged over a period) as α increases for $R_s = 10$ and $\delta = 0, 0.1$ and 0.3. The boundary-layer width is based on the streamfunction properties and is defined to be the distance from $r = 1$ of the point lying on $\theta = \pi/2$ where ψ passes through zero. The dash-dot-dot-dot line is proportional to α^{-1} for comparison. Solid curve, $\delta = 0$; dotted curve, $\delta = 0.1$; dashed curve, $\delta = 0.3$.

Note that in postulating these solutions we are ruling out the possibility of asymmetric solutions. Assuming that there are no secular terms in time, i.e. that the variables are all sinusoidal in time, or constant, we may decompose ψ_0 into a steady and a sinusoidal component. Thus, we write $\psi_0 = \psi_0^s + \psi_0^u$ where ψ_0^s is time-independent, and $\int_0^{2\pi} \psi_0^u \mathrm{d}t = 0$. Equation (4.4*a*) and the time average of (4.4*c*) lead to

$$\mathscr{L}\psi_0^u = 0, \quad \frac{1}{r}\mathscr{J}\left(\frac{\mathscr{L}\psi_0^s}{h}, h\psi_0^s\right) = \mathscr{L}^2\psi_0^s, \tag{4.5}$$

As expected, $w_0 = \sqrt{2R_s}h^{-1}\sin t$ does not satisfy the no-slip boundary condition, and it is necessary to consider a boundary layer of thickness α^{-1} near the wall. We introduce the boundary-layer coordinate $r = 1 - \eta/\alpha$ and seek solutions in the

boundary layer of the form $w = \alpha W_0 + W_1 + \cdots$, $\psi = \alpha^{-1}\Psi_0 + \alpha^{-2}\Psi_1 + \cdots$. At $O(\alpha^3)$, equations (2.7) and (2.9) give

$$\frac{\partial W_0}{\partial t} = \frac{\sqrt{2R_s}}{h_0}\cos t + \frac{\partial^2 W_0}{\partial \eta^2}, \quad \frac{\partial^3 \Psi_0}{\partial t \partial \eta^2} + \frac{1}{h_0} W_0 \frac{\partial W_0}{\partial \eta}\sin\theta = \frac{\partial^4 \Psi_0}{\partial \eta^4}, \tag{4.6}$$

where $h_0 = 1 + \delta\cos\theta$. The solution for W_0 satisfying the no-slip boundary condition $W_0 = 0$ at $\eta = 0$ and matching with the core solution (equation (4.3)) is

$$W_0 = \frac{\sqrt{2R_s}}{h_0}\left(\sin t + \mathrm{e}^{-\eta/\sqrt{2}}\sin\left(\frac{\eta}{\sqrt{2}} - t\right)\right). \tag{4.7}$$

Similarly, the solution for Ψ_0 satisfying the no-slip boundary conditions $\Psi_0 = \partial\Psi_0/\partial\eta = 0$ at $\eta = 0$ and matching with the core solution is

$$\begin{aligned}\Psi_0 = \frac{R_s \sin\theta}{\sqrt{2}h_0^3}\Bigg(&-\tfrac{1}{8}\exp\left(-\sqrt{2}\eta\right)\left[2 + \sin(\sqrt{2}\eta - 2t) + \cos(\sqrt{2}\eta - 2t)\right] \\ &- \exp\left(-\frac{\eta}{\sqrt{2}}\right)\left[\sin\left(\frac{\eta}{\sqrt{2}}\right) + \cos\left(\frac{\eta}{\sqrt{2}}\right) + \sin\left(\frac{\eta}{\sqrt{2}} - 2t\right) + \cos\left(\frac{\eta}{\sqrt{2}} - 2t\right)\right] \\ &+ \frac{5}{4\sqrt{2}}\exp(-\eta)\left[\sin(\eta - 2t) + \cos(\eta - 2t)\right] + \tfrac{5}{4} - \tfrac{1}{4}\sqrt{2}\eta \\ &+ \tfrac{1}{8}(9 - 5\sqrt{2})(\cos(2t) - \sin(2t))\Bigg).\end{aligned} \tag{4.8}$$

Hence we see that as $\eta \to \infty$, not only does Ψ_0 not tend to zero but neither does $\partial\Psi_0/\partial\eta$. Matching with the core solution gives $\psi_0^s = 0$ and $\partial\psi_0^s/\partial r = R_s \sin\theta/4h_0^3$ at $r = 1$.

Writing $\psi_0^s = R_s\chi$, the governing equation for the steady secondary flow in the core becomes

$$\frac{1}{r}\mathscr{J}\left(\frac{\mathscr{L}\chi}{h}, h\chi\right) = \frac{1}{R_s}\mathscr{L}^2\chi, \tag{4.9}$$

subject to the boundary conditions

$$\chi = 0, \quad \frac{\partial\chi}{\partial r} = \frac{\sin\theta}{4h_0^3} \quad \text{at} \quad r = 1, \tag{4.10}$$

from which it becomes clear that R_s is the secondary streaming Reynolds number. We also define the rescaled axial vorticity, $\omega = -\mathscr{L}\chi$.

To determine how large α must be for the asymptotic approximation to the boundary-layer flow to be accurate, we compare the numerical results from § 4.2 with the leading-order parts of the analytical solutions for the boundary-layer flow, given in (4.7) and (4.8). The leading-order component of the streamfunction in the boundary layer is $\alpha^{-1}\Psi_0$ (see equation (4.3)), and inspection of Ψ_0 (equation (4.8)) reveals that, along the line $\theta = \pi/2$, Ψ_0/R_s is independent of α, R_s and δ (since $h_0 = 1$ when $\theta = \pi/2$). Thus we expect that, for a given value of η and at $\theta = \pi/2$, and as $\alpha \to \infty$, $\alpha R_s^{-1}\psi$ will converge to a finite value that is independent of R_s and δ. Plots showing comparisons between the asymptotic and numerical values of the time average of $\alpha R_s^{-1}\psi$ are shown in figure 12(*a*). The solid line corresponds to the asymptotic solution, while the remaining curves correspond to the numerical solutions for $\alpha = 20$, 60, and $\delta = 0$, 0.3. For both $\alpha = 20$ and $\alpha = 60$, the curves for $\delta = 0$ and $\delta = 0.3$ are almost identical, indicating that for large α, the boundary-layer streamfunction is almost independent of δ as expected, and as α increases, the numerical solutions approach the asymptotic solution.

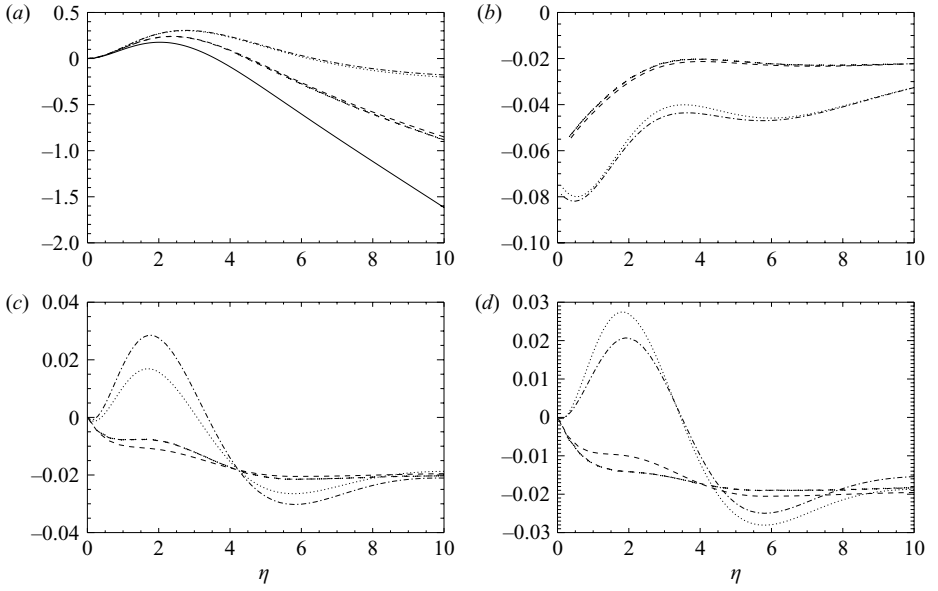

FIGURE 12. Plots showing a comparison of the numerical results with the analytical solution in the asymptotic limit as $\alpha \to \infty$. In all the figures, the numerical results are shown by: dotted curve, $\alpha = 20$, $\delta = 0$; dashed curves, $\alpha = 60$, $\delta = 0$, dash-dot curves: $\alpha = 20$, $\delta = 0.3$; dash-dot-dot-dot curves, $\alpha = 60$, $\delta = 0.3$; all numerical results are for $R_s = 10$. (*a*) Time-average of $\alpha R_s^{-1}\psi$ along the line $\theta = \pi/2$. The solid curve shows the asymptotic solution. (*b*) Time-average of $\alpha^{-1}R_s^{-1}\xi$ along the line $\theta = \pi/2$. The curves show the relative difference between the numerical and asymptotic values, which is defined to be (numerical value − asymptotic value)/(maximum asymptotic value − minimum asymptotic value). (*c*) and (*d*), axial velocity $\alpha^{-1}R_s^{-1/2}h_0 w$ at $t = 0$ along the lines $\theta = 0$ and $\theta = \pi$, respectively. The curves show the relative difference between the numerical and asymptotic values, defined to be (numerical value − asymptotic value)/(maximum asymptotic value), since they were almost indistinguishable on a graph of numerical and asymptotic values.

In a similar way, for $\theta = \pi/2$ and fixed η, we expect $\alpha^{-1}R_s^{-1}\xi$ to converge to a finite value that is independent of R_s and δ; plots of the relative difference between the time-average of the numerical solution and the asymptotic solution are shown in figure 12(*b*). The numerical solutions stay remarkably close to the asymptotic solution well into the interior of the pipe (the variation of ξ in the radial direction along the line $\theta = \pi/2$ is shown in figure 9 for $\alpha = 20$, $R_s = 10$ and $\delta = 0, 0.3$).

Finally, as $\alpha \to \infty$, $\alpha^{-1}R_s^{-1/2}h_0 w$ converges to a finite value that is independent of R_s, δ and θ. The relative difference between the numerical and asymptotic values of this quantity at $t = 0$ are plotted in figures 12(*c*) and 12(*d*) for $\theta = 0$ and $\theta = \pi$, respectively (the variation of w in the radial direction along the line $\theta = 0$ is shown in figure 9 for $\alpha = 20$, $R_s = 10$ and $\delta = 0, 0.3$). Again, the numerical solutions stay remarkably close to the asymptotic solution well into the pipe interior. The results suggest that, even at $\alpha = 20$, the solution is fairly close to the boundary-layer solution in the limit $\alpha \to \infty$ for $\eta \lesssim 1$ (and indeed for larger η also).

4.3.1. *Analytical solution for steady secondary core flow (small R_s and δ)*

When $R_s \ll 1$ and $\delta \ll 1$, it is possible to find a series solution to (4.9) which must be solved subject to (4.10). We write $\chi = \sum_{m=0}^{\infty} R_s^m \chi_m$, where $\chi_m = \sum_{n=0}^{\infty} \delta^n \chi_{mn}$. The

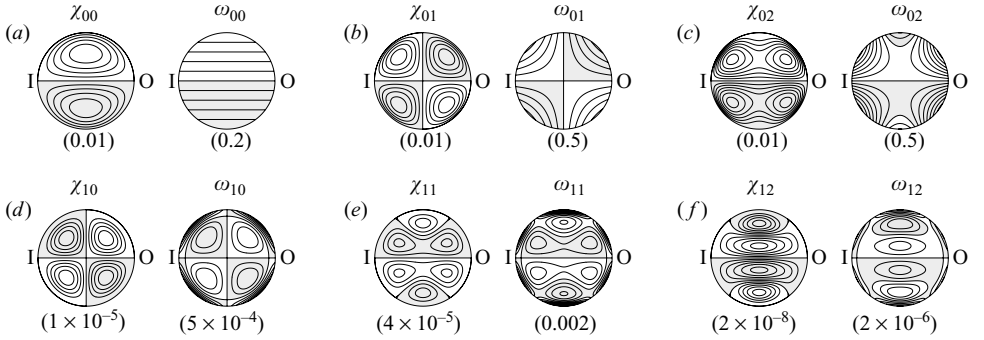

FIGURE 13. Streamlines and axial vorticity contours showing the components of the core flow for $\alpha \gg 1$. The solutions shown in (*a*), (*d*) and (*f*) were also found by Lyne (1971) and Stuart (1966).

boundary conditions at $r=1$ become $\chi_m = 0\ \forall m$ together with

$$\frac{\partial \chi_0}{\partial r} = \tfrac{1}{4}\sin\theta - \tfrac{3}{8}\delta\sin 2\theta + \tfrac{3}{8}(\sin\theta + \sin 3\theta)\,\delta^2 - \tfrac{5}{16}(2\sin 2\theta + \sin 4\theta)\,\delta^3 + O(\delta^4), \quad (4.11)$$

and $\partial\chi_m/\partial r = 0$ for $m > 0$.

Equation (4.8) at $O(R_s^{-1})$ gives $\mathscr{L}^2\chi_0 = 0$. The first three terms in the series solution are

$$\chi_{00} = -\frac{r}{8}(1-r^2)\sin\theta, \quad \chi_{01} = \frac{3r^2}{16}(1-r^2)\sin 2\theta, \quad (4.12)$$

$$\chi_{02} = -\frac{3r}{256}(11+5r^2)(1-r^2)\sin\theta - \frac{3r^3}{16}(1-r^2)\sin 3\theta. \quad (4.13)$$

These solutions are shown in figure 13(*a–c*) together with the corresponding axial vorticity contours, where we have expanded $\omega = \sum_{m,n\geqslant 0} R^m\delta^n\omega_{mn}$. At leading order, the secondary flow consists of two vortices, with flow from the outside of the bend of the pipe ($\theta = 0$) to the inside ($\theta = \pi$), and back around the walls. The corresponding vorticity contours indicate that the vorticity is constant along horizontal lines. As δ increases, the primary effect, due to the χ_{01} term, is to move the vortex centre towards the inside of the pipe wall, and the secondary effect due to the χ_{02} term is to slow the flow (by flattening the streamfunction) near the centre and speed it up round the edges.

Equation (4.8) at $O(1)$ gives $\mathscr{L}^2\chi_1 = r^{-1}\mathscr{J}(h^{-1}\mathscr{L}\chi_0, h\chi_0)$, and expanding in powers of δ, we find that

$$\chi_{10} = -\frac{r^2}{2^{10}\times 3}(1-r^2)^2\sin 2\theta, \quad (4.14)$$

$$\chi_{11} = \frac{r}{2^{10}\times 3^2}(4-7r^2)(1-r^2)^2\sin\theta + \frac{77r^3}{2^{12}\times 5\times 3}(1-r^2)^2\sin 3\theta. \quad (4.15)$$

Contours of these streamfunctions together with the corresponding axial vorticity are shown in figures 13(*d*) and 13(*e*). Finally, at $O(R_s)$, we have

$$\mathscr{L}^2\chi_2 = \frac{1}{r}\mathscr{J}\left(\frac{\mathscr{L}\chi_0}{h}, h\chi_1\right) + \frac{1}{r}\mathscr{J}\left(\frac{\mathscr{L}\chi_1}{h}, h\chi_0\right), \quad (4.16)$$

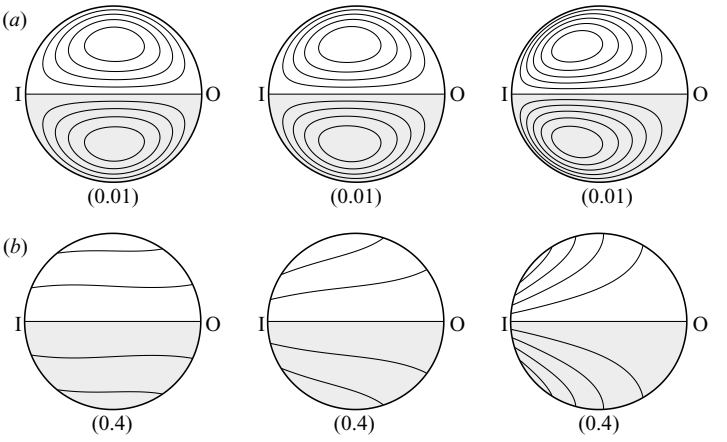

FIGURE 14. (*a*) Streamfunction contours and (*b*) axial vorticity contours for $\delta = 0$, $\delta = 0.1$ and $\delta = 0.3$, respectively. All results are for $R_s = 10$.

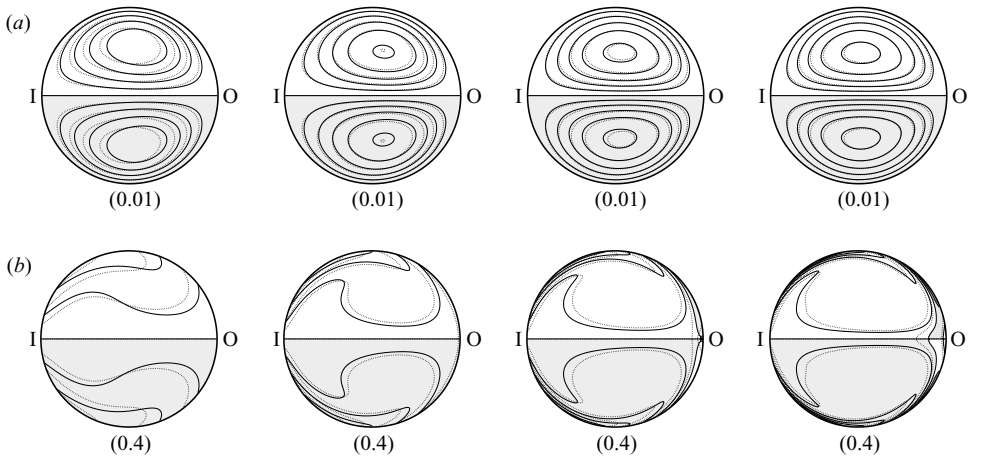

FIGURE 15. (*a*) Streamfunction contours and (*b*) axial vorticity contours for $R_s = 100$, $R_s = 400$, $R_s = 1000$ and $R_s = 2000$, respectively. Solid curves, $\delta = 0$; dotted curves, $\delta = 0.1$.

and we find

$$\chi_{20} = -\frac{r}{2^{16} \times 5 \times 3^2}(2 - 7r^2 + 4r^4)(1 - r^2)^2 \sin\theta - \frac{r^3}{2^{15} \times 5 \times 3^2}(1 - r^2)^2 \sin 3\theta. \quad (4.17)$$

Figure 13(*f*) shows contours of χ_{20} and the corresponding axial vorticity. As R_s increases (for $\delta = 0$), the leading-order effect, due to χ_{10}, is to move the centre of the vortex towards the outside of the pipe bend (figure 13*d*).

4.3.2. *Numerical solution for steady secondary core flow (intermediate values of R_s and δ)*

At larger values of R_s and δ, we must solve (4.9) subject to (4.10) numerically. We add a fictitious time variable, and solve the system using the implicit Euler method and the spatial discretization described in § 4.1. Figure 14 shows the effect of increasing δ whilst keeping $R_s = 10$. As δ increases, the vortices move towards the inside of the pipe bend, which agrees with the behaviour of χ_0 predicted analytically in § 4.3.1. In figure 15, streamlines and axial vorticity contours are shown for $R_s = 100$, 400,

1000 and 2000 and two different values of δ. Comparing the solutions for $R_s = 10$ and $R_s = 100$, we see that the centre of the vortex at $R_s = 100$ is further towards the outside of the pipe bend, in agreement with the asymptotic predictions of § 4.3.1. The effect is still noticeable at $R_s = 400$, but as R_s increases further, the vortex centre moves back towards $\theta = \pi/2$, and by $R_s = 2000$, the streamlines are almost symmetrical in the vertical axis, as reported by van Meerveld & Waters (2001). The axial vorticity contours become progressively more skewed, and for $R_s \gtrsim 1000$, boundary layers begin to form around the walls and across the horizontal axis.

As δ increases, for smaller values of R_s the centre of the vortex moves towards the inside of the bend, as predicted in § 4.3.1. At $R_s = 2000$, the streamlines for $\delta = 0$ and $\delta = 0.1$ are virtually identical. However, close inspection of the vorticity boundary layers reveals that the curves for $\delta = 0.1$ lie slightly further away from the wall than those for $\delta = 0$, and thus the boundary layer is slightly thicker for the larger-δ case. The numerical results also indicate that, for fixed values of δ, the width of the boundary layer scales as $R_s^{-1/2}$ (van Meerveld & Waters 2001).

We remark again that we have ruled our asymmetric solutions by our assumptions, and since it was difficult to resolve numerical solutions to the full problem when α and R_s are both large, we are not able to determine the nature of the bifurcation diagram at large values of α. The possibility exists therefore that the symmetric flows presented in figure 14 for large R_s may be unstable to asymmetric perturbations. However, further analysis to determine the stability of these flows is beyond the scope of the paper.

5. Oscillatory pressure gradient

Our focus here is to determine the effect of adding a steady component of the axial pressure gradient on the types of flow found in § 4.2; in particular, we seek to quantify the effect of the steady driving pressure gradient component on the spatially asymmetric solutions found in that section.

We start by considering the flow corresponding to $D = 0$, $\alpha = 10$ and $R_s = 50$. We consider $\delta = 0, 0.1$ and 0.3; from figure 4, we see that the branch 1 solution (periodic and symmetric) is stable at these parameter values. Streamlines and contour plots of the axial velocity and axial vorticity during the first half-period are shown in figure 16. The spatially symmetric solutions also possess a temporal symmetry in which the solution is translated forward by half a period and the sign of the axial velocity is reversed. If we now increase the Dean number, this temporal symmetry is lost, as expected. Plots corresponding to $D = 500$ and 5000 are given in figures 17 and 18, respectively. For large values of D, we see that the solution adopts many characteristics of steady flows at high Dean numbers (Siggers & Waters 2005). In particular, a boundary layer forms at $r = 1$, which can be seen in the plots of axial velocity, axial vorticity and, to a lesser extent, in the streamfunction. Moreover, the axial velocity contours become approximately vertical and the axial vorticity is almost constant in the core. Additional transient vortices in the streamfunction are also evident at large Dean numbers; see for example the streamfunction at $t = 5\pi/3$ in figure 18.

Next we consider the asymmetric solution with $D = 0$, $\delta = 0$, $\alpha = 10$ and $R_s = 120$, shown in figure 7. As D is increased from zero, the solutions automatically loses its temporal symmetry as expected, and then, at a critical value of D, which lies between 425 and 430 (for these values of δ, α and R_s), the solution regains spatial symmetry via a pitchfork bifurcation (see figure 19).

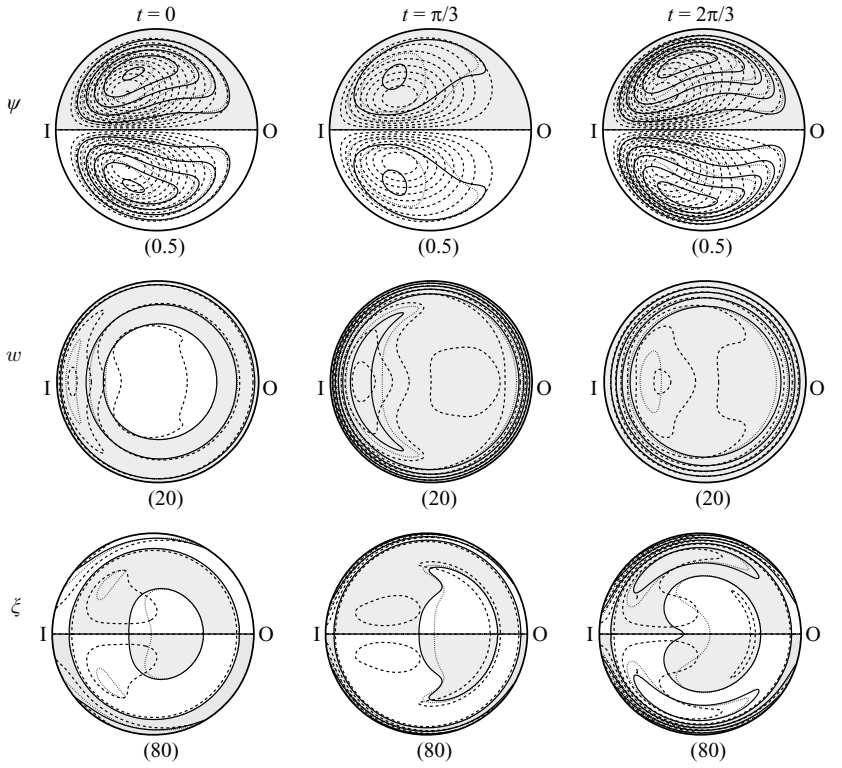

FIGURE 16. Contour plots of solutions found with $D = 0$, $R_s = 50$, $\alpha = 10$ and $\delta = 0, 0.1$ and 0.3, shown at $t = 0, \pi/3, 2\pi/3$. Solid curves, $\delta = 0$; dotted curves, $\delta = 0.1$; dashed curves, $\delta = 0.3$.

Siggers & Waters (2005) showed that when the flow is driven by a steady pressure gradient, there are always stable steady solutions that are symmetric in $\theta = 0, \pi$. When a small time-dependent component is added to the pressure gradient, these solutions will correspond to the branch 1 solutions shown in figure 3. Thus, in general, we expect for sufficiently large D, branch 2 and 3 solutions will converge onto these (symmetric) solutions, since the effect of the time-dependent component of the pressure gradient becomes relatively small.

6. Effect of curvature on the wall shear stress

In this section, we quantify the effect of pipe curvature on the shear stress distribution, given by (2.10). For simplicity, we restrict attention to branch 1 solutions. We wish to vary the curvature, δ, whilst keeping the dimensional pressure gradient (characterized by P_0, K and T), the fluid properties (characterized by ρ and ν), and the pipe radius (characterized by a) fixed. By writing $D = 4\sqrt{2\delta Re}$ where $Re = P_0 a^3/(4\rho\nu^2)$, and $R_s = \delta\widetilde{R_s}$ where $\widetilde{R_s} = K^2T^3/(\nu\rho^2)$, it becomes clear that the desired parameter study is achieved by fixing the parameters Re, $\widetilde{R_s}$ and α at constant values whilst varying δ (note that D and R_s will vary accordingly). This parameter study is more physiologically relevant than that obtained by fixing D, R_s and α, and will be discussed in the remainder of this section.

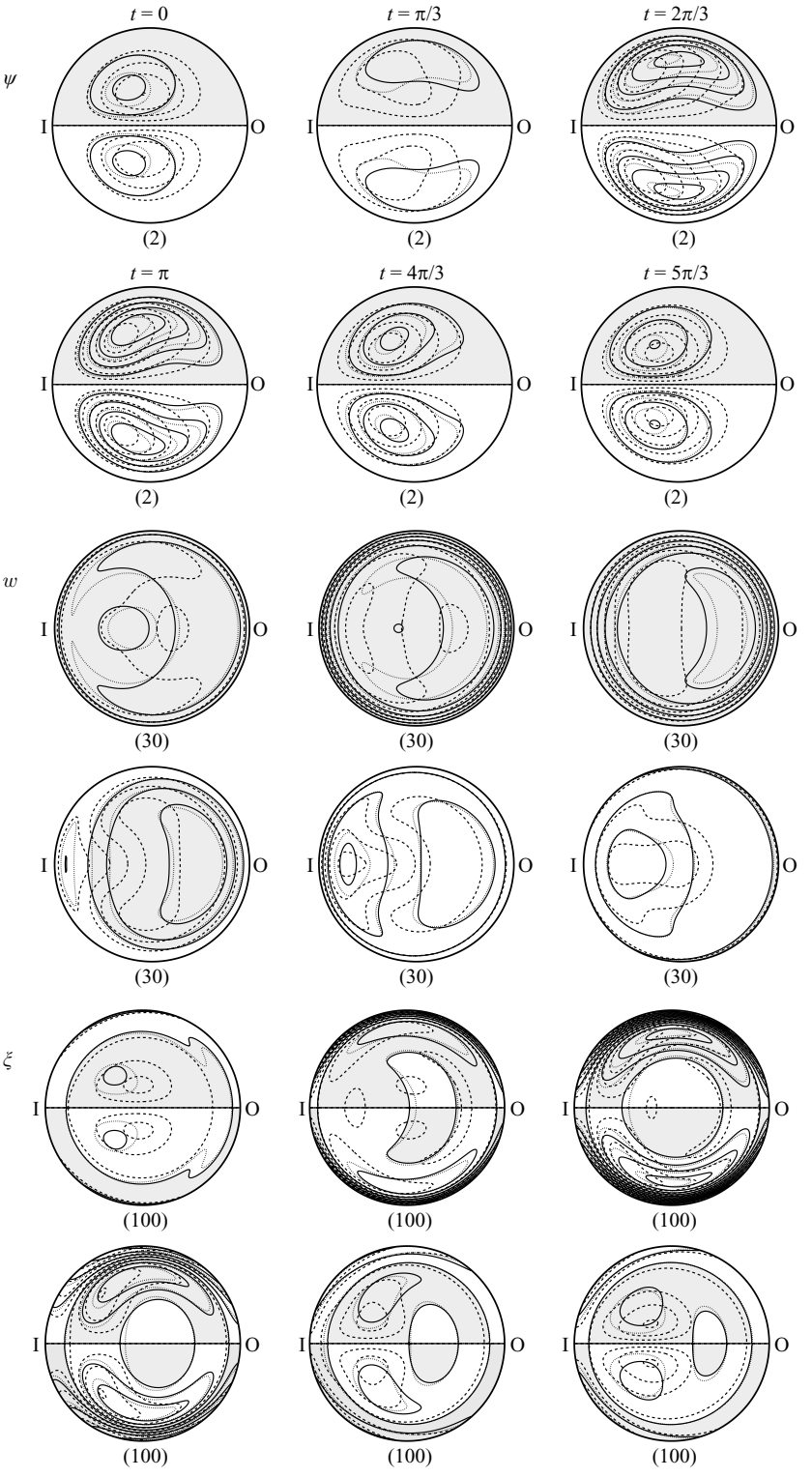

FIGURE 17. Contour plots of solutions found with $D = 500$, $R_s = 50$, $\alpha = 10$ and $\delta = 0$, 0.1 and 0.3, each shown at six equally spaced time points over the period. Solid curves, $\delta = 0$; dotted curves, $\delta = 0.1$; dashed curves, $\delta = 0.3$. The shading indicates regions where the solution with $\delta = 0$ is positive.

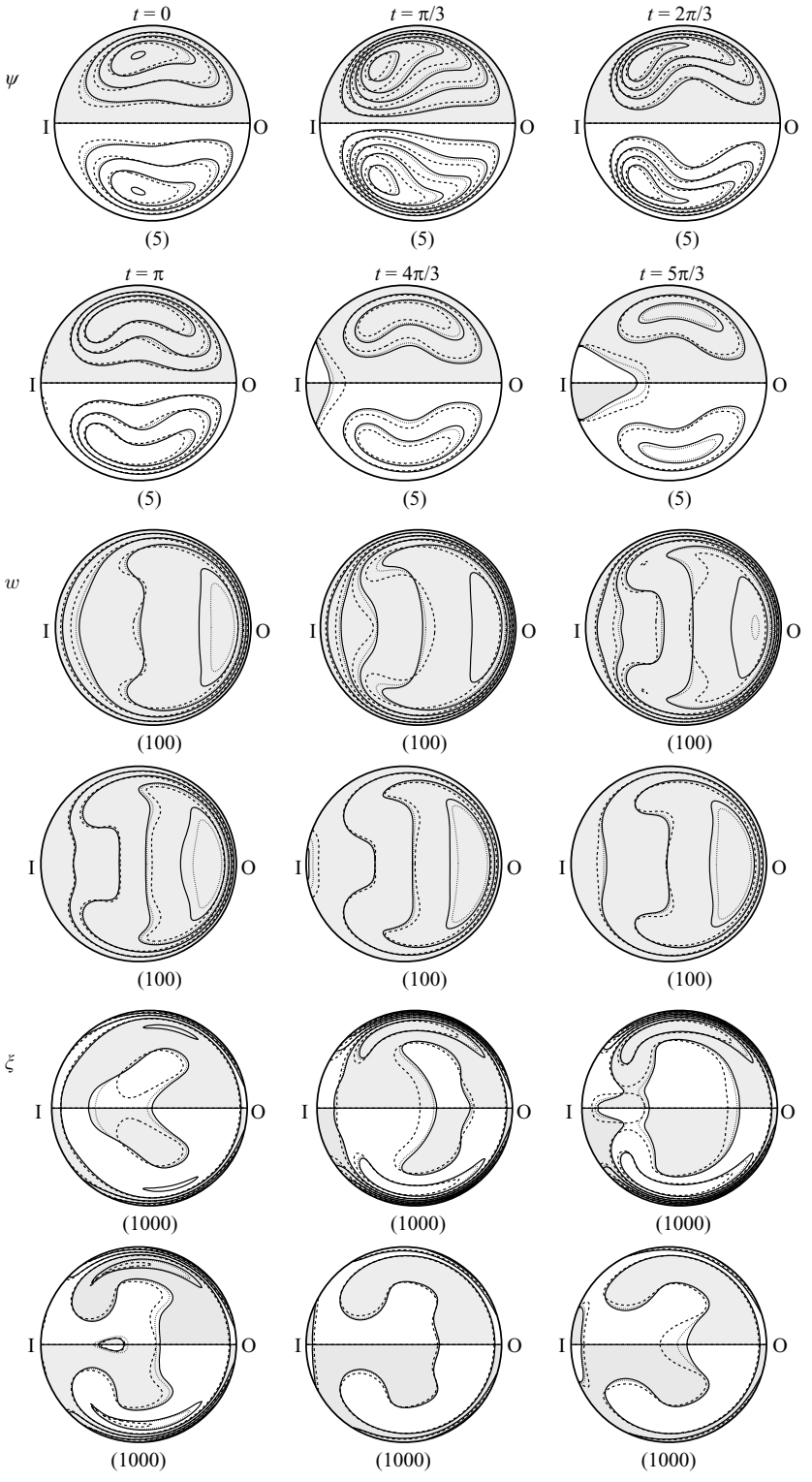

FIGURE 18. Contour plots of solutions found with $D = 5000$, $R_s = 50$, $\alpha = 10$ and $\delta = 0, 0.1$ and 0.3, each shown at six equally spaced time points over the period. Solid curves, $\delta = 0$; dotted curves, $\delta = 0.1$; dashed curves, $\delta = 0.3$.

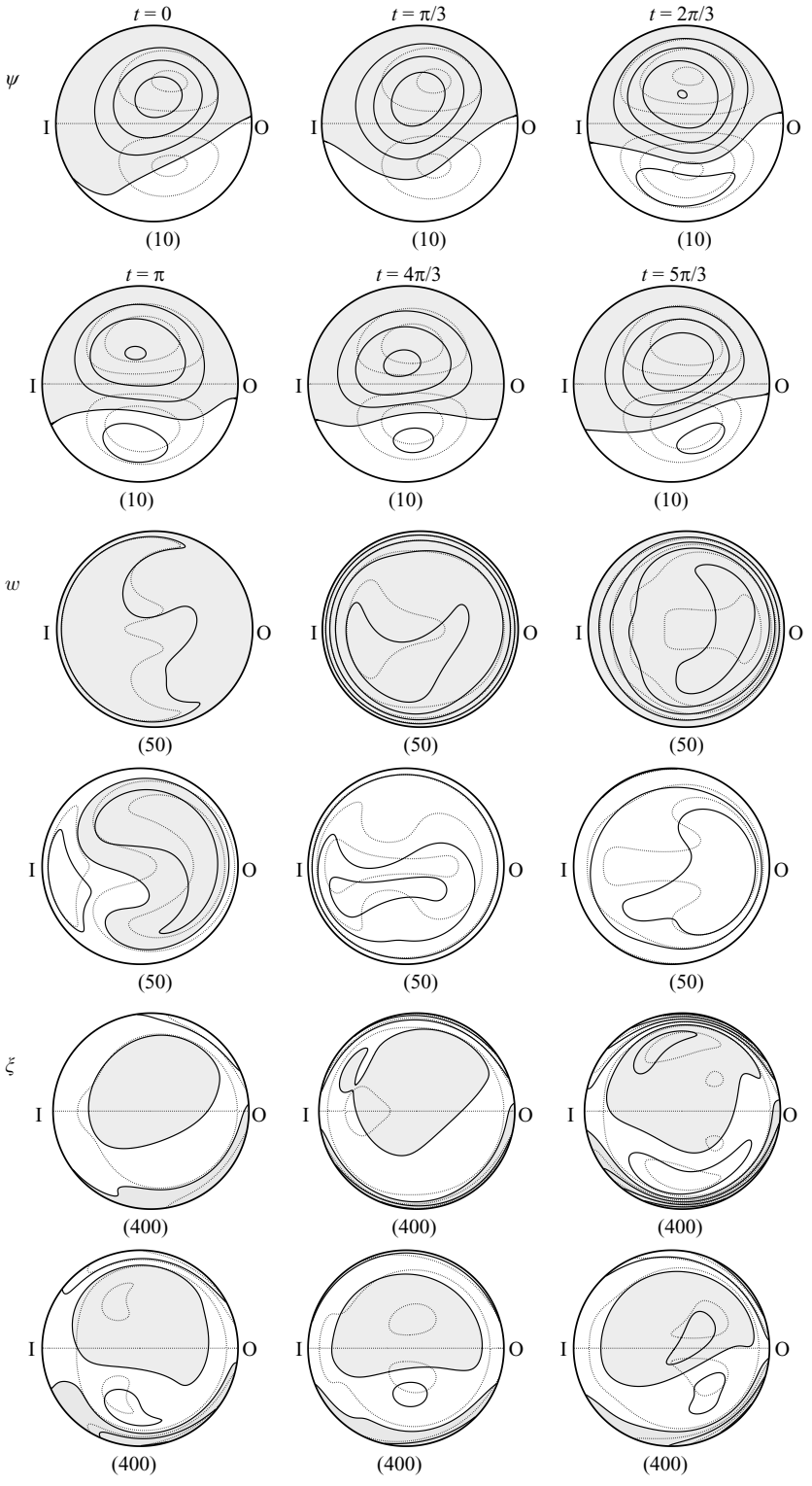

FIGURE 19. Contour plots of solutions found with $R_s = 120$, $\alpha = 10$ and $\delta = 0$, shown at six equally spaced time points over the period. Solid curves, $D = 425$; dashed curves, $D = 430$. Shaded areas indicate regions where the solutions with $D = 425$ are positive.

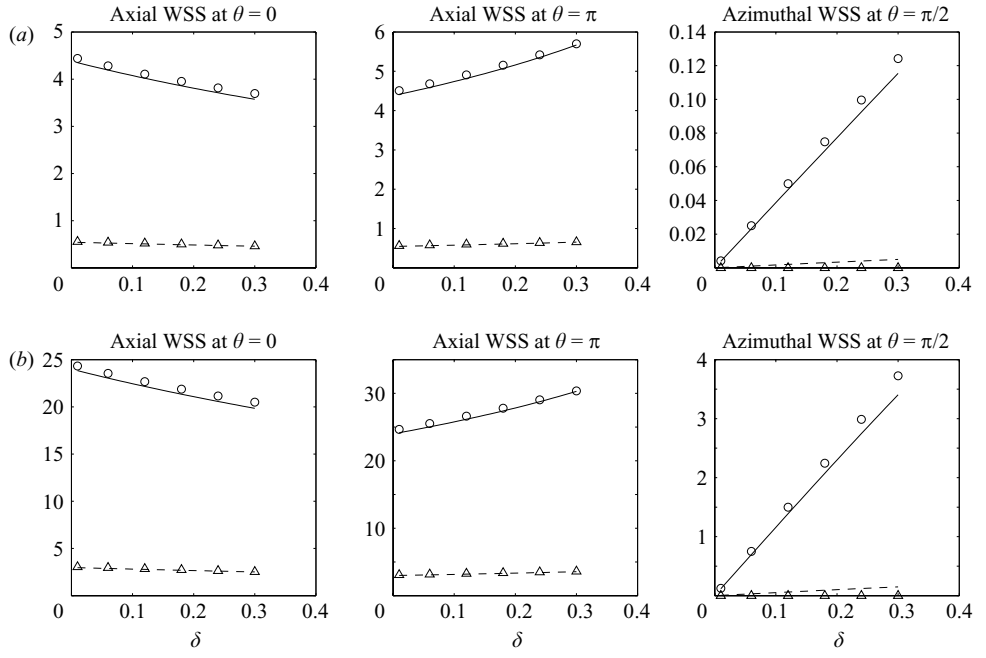

FIGURE 20. Graphs showing how the WSS properties vary as δ changes. (a) $\alpha = 1$, $\widetilde{R_s} = 80$; (b) $\alpha = 1$, $\widetilde{R_s} = 2400$, both with $Re = 0$. Solid curves, numerical solutions for $t = 0$; dashed curves, numerical solutions for $t = \pi/2$; circles and triangles denote analytical solutions found in § 3 for $t = 0$ and $t = \pi/2$, respectively.

Initially, we consider the sinusoidal case ($Re = 0$), and in figure 20 present some representative WSS plots. Recall that, at least in the asymptotic case presented in § 3, the time-averaged axial WSS attains its maximum and minimum values at $\theta = 0$ and $\theta = \pi$ (see (3.17)), whilst the azimuthal WSS attains its maximum close to $\theta = \pi/2$ (see (3.18)). Motivated by this we present the axial WSS at $\theta = 0$ and $\theta = \pi$ and the azimuthal WSS at $\theta = \pi/2$ in figure 20 at $t = 0$ and $t = \pi/2$. Figures 20(a) and 20(b) show a comparison between the numerical results and the asymptotic estimates that were found in § 3, for $\alpha = 1$ and $\widetilde{R_s} = 80$ and 2400, respectively. The numerical and asymptotic values remain very close as δ increases away from zero, even up to $\delta = 0.3$. There is a significant change in both the axial and azimuthal WSS at $t = 0$ as δ varies from 0 to 0.3.

We also consider the variation of the WSS distribution with δ for the case where the flow is driven by an oscillatory pressure gradient with $Re \neq 0$. In figure 21, we present the maximum and minimum values of the axial WSS at the outer and inner walls and the azimuthal WSS at $\theta = \pi/2$. For $Re = 5$, $\alpha = 1$ and $\widetilde{R_s} = 80$ (figure 21a), we also see that there is excellent agreement between the analytical and numerical results as δ varies between 0 and 0.3. However, in figure 21(b), which corresponds to $\alpha = 2$, we see that the agreement between the analytical and numerical results is less satisfactory; we remark that this rapid decrease in agreement is expected since the analytical results are proportional to α^3. We again remark that there is significant variation in the WSS distribution with δ.

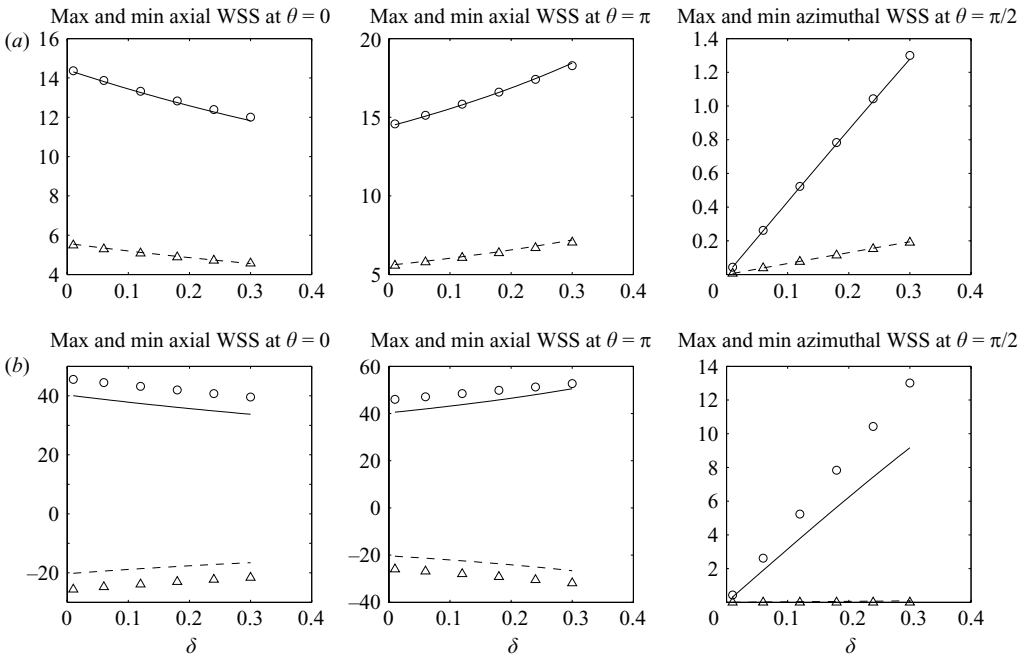

FIGURE 21. Effect of varying δ on the WSS of solutions driven by an oscillatory pressure gradient. (*a*) $Re = 5$, $\alpha = 1$, $\widetilde{R_s} = 80$, (*b*) $Re = 5$, $\alpha = 2$, $\widetilde{R_s} = 80$. Solid curves, numerical results for maximum value during cycle; dashed curves, numerical results for minimum during cycle; circles and triangles denote analytical solutions from § 3 for maximum and minimum, respectively.

7. Conclusions

In this paper, we considered flows driven by oscillatory pressure gradients in pipes with finite curvature. The flow behaviour is governed by four dimensionless parameters: the curvature, δ; the Dean number, D; the Womersley number, α; and the secondary streaming Reynolds number, R_s. Analytical solutions were obtained when each of the curvature, the driving pressure gradient and α were small, and also in the case when $\alpha \gg 1$ and R_s and δ are small. A pseudospectral code was used to obtain solutions at finite values of the governing parameters; a key feature of our numerical scheme was that it enabled us to seek solutions that are spatially asymmetric in the pipe centreplane.

For flows driven by sinusoidal pressure gradients with $\alpha = 10$, we identified three distinct classes of stable solution: periodic and symmetric (branch 1); periodic and asymmetric (branch 2); and asymmetric solutions that are not 2π periodic (branch 3). When the branch 1 solutions lose stability they undergo a transition to either branch 2 or branch 3 solutions, depending on the value of δ. For δ less than a certain critical value, branch 1 solutions will undergo a transition to branch 2 solutions; however, above the critical value of δ, the branch 1 solutions will undergo a transition to branch 3 solutions. Thus, the *qualitative* solution structure is sensitive to the value of δ. As D increases from zero, the temporal symmetry of solutions is automatically broken. However, it does not initially affect the spatial symmetry of solutions, although for higher values of D, some branch 2 solutions were found to regain spatial symmetry.

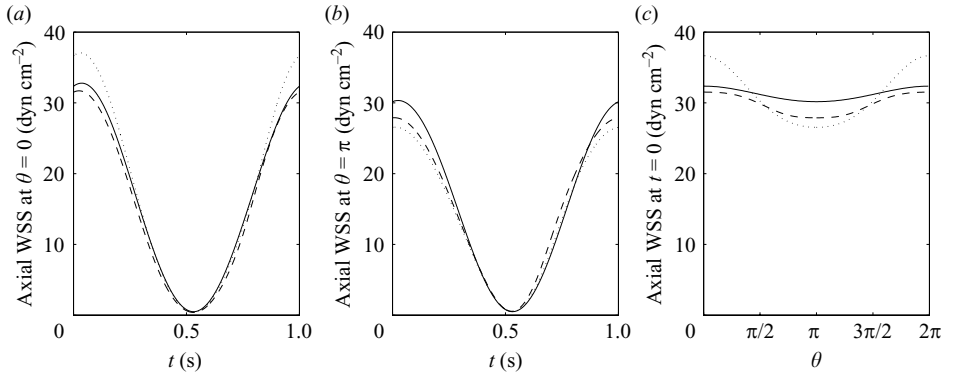

FIGURE 22. Dimensional axial wall shear stress, showing the dependence on curvature. The remaining parameter values are chosen to be representative of those in the major coronary arteries branching off the aortic arch. In this figure $a = 10^{-3}$ m, $T = 1/(2\pi)$ s, $\nu = 4 \times 10^{-6}$ m^2 s^{-1}, $Re = 50$ and $\tilde{R}_s = 3.2 \times 10^5/\pi^3$ (hence $\alpha = \sqrt{\pi/2}$), (with $\delta = 1/4$ this gives typical physiological values). Solid curves, $\delta = 0.01$; dotted curves, $\delta = 0.1$; dashed curves: $\delta = 0.3$. Axial WSS at (a) the outer wall as a function of time, (b) the inner wall as a function of time, and (c) at $t = 0$ as a function of θ.

Zabielski & Mestel (1998*a*, *b*) considered a related problem of helically symmetric flows in helical pipes wound around the Cartesian z-axis. The equations were shown to admit the following spatio-temporal symmetry

$$w(\tilde{r}, \phi, t + \pi) = -w(\tilde{r}, -\phi, t), \quad \psi(\tilde{r}, \phi, t + \pi) = -\psi(\tilde{r}, -\phi, t), \tag{7.1}$$

where $\tilde{r}$ and ϕ are polar coordinates in the plane of the pipe cross-section. For flows driven by an oscillatory pressure gradient, Zabielski & Mestel found that solutions breaking this symmetry exist for a finite range of amplitudes of the pressure gradient. This is in contrast to our study, where the term 'symmetric' refers to solutions that are spatially symmetric in the pipe centreplane at all times, i.e.

$$w(r, \theta, t) = w(r, -\theta, t), \quad \psi(r, \theta, t) = -\psi(r, -\theta, t). \tag{7.2}$$

(The helical geometry of Zabielski & Mestel rules out the analogous symmetry in their work.)

Our study was motivated by blood flow in arteries, and, in particular, how the WSS distribution depends on the vessel curvature. Suppose we consider major arteries branching off the aorta with radius approximately $a = 1 \times 10^{-3}$ m. If we assume the period of the heart beat, $2\pi T$, is 1 s, and the kinematic viscosity of blood is $\nu = 4 \times 10^{-6}$ m^2 s^{-1} (Pedley 1980; Sugawara *et al.* 1989) then we obtain a Womersley number $\alpha = \sqrt{\pi/2}$. Taking the mean blood velocity to be 0.1 m s^{-1} we obtain an estimate for the Reynolds number, Re, of approximately 50. We assume that the amplitude of the sinusoidal component of the pressure gradient, K, is equal to the steady component of the pressure gradient, P_0, which gives an estimate for $\widetilde{R_s}$ of $3.2 \times 10^5/\pi^3$. Using these parameter estimates, the dimensional axial WSS at the outer and inner walls as a function of time is shown in figures 22(a) and 22(b). Additionally, we plot the dimensional axial WSS at $t = 0$ in figure 22(c). In general the WSS does not vary monotonically with δ: this non-monotonic behaviour emphasises the importance of incorporating the effects of finite curvature into the model.

Finally, the existence of asymmetric solutions is potentially physiologically significant, as the resulting circumferential distribution of WSS will reflect the

asymmetry (plaques are observed to develop asymmetrically). At the parameter values considered here, we found only a symmetric solution, although we cannot rule out the existence of additional solution branches.

We would like to thank Andrew Hazel, Matthias Heil, Paul Matthews and Jonathan Mestel for helpful comments and discussions. The majority of this work was carried out while J. H. S. and S. L. W. were at the University of Nottingham. J. H. S. was supported by the EPSRC grant GR/R89301/01. SLW is grateful for support from the MRC (Discipline Hopping Award) and the EPSRC (Advanced Research Fellowship). During this work, we made use of computational facilities provided by the EPSRC JREI scheme, grant GR/R08292/01.

REFERENCES

Berger, S. A., Talbot, L. & Yao, L.-S. 1983 Flow in curved tubes. *Annu. Rev. Fluid Mech.* **15**, 461–512.

Blennerhassett, P. J. 1976 Secondary motion and diffusion in unsteady flow in a curved pipe. PhD thesis, Imperial College, London.

Caro, C. G., FitzGerald, J. M. & Schroter, R. C. 1971 Atheroma and arterial wall shear – observation, correlation and proposal of a shear dependent mass transfer mechanism for atherogenesis. *Proc. R. Soc. Lond.* B **177**, 109–159.

Chandran, K. B., Yearwood, T. L. & Wieting, D. W. 1979 An experimental study of pulsatile flow in a curved tube. *J. Biomech.* **12**, 793–805.

Chang, L.-J. & Tarbell, J. M. 1985 Numerical simulation of fully developed sinusoidal and pulsatile (physiological) flow in curved tubes. *J. Fluid Mech.* **161**, 175–198.

Dean, W. R. 1928 The stream-line motion of fluid in a curved pipe. *Phil. Mag.* **5**, 673–695.

Glendinning, P. 1994 *Stability, Instability and Chaos: an Introduction to the Theory of Nonlinear Differential Equations*. Cambridge University Press.

Haddon, E. W. 1982 A high Reynolds number flow with closed streamlines. In *Eighth Intl Conf. on Numerical Methods in Fluid Dynamics, Aachen*. Lecture Notes in Physics, vol. 170. Springer.

Hamakiotes, C. C. & Berger, S. A. 1990 Periodic flows through curved tubes – the effect of the frequency parameter. *J. Fluid Mech.* **210**, 353–370.

Ito, H. 1987 Flow in curved pipes. *JSME Intl J.* **30**, 543–552.

Lin, J. Y. & Tarbell, J. M. 1980 An experimental and numerical study of periodic flow in a curved tube. *J. Fluid Mech.* **100**, 623–638.

Lyne, W. H. 1971 Unsteady viscous flow in a curved pipe. *J. Fluid Mech.* **45**, 13–31.

van Meerveld, J. & Waters, S. L. 2001 Numerical computation of the steady secondary flow in a tube with time-dependent curvature. *Q. J. Mech. Appl. Maths* **54**, 631–640.

Mullin, T. & Greated, C. A. 1980 Oscillatory flow in curved pipes. Part 2. The fully developed case. *J. Fluid Mech.* **98**, 397–416.

Pedley, T. J. 1980 *The Fluid Mechanics of Large Blood Vessels*. Cambridge University Press.

Siggers, J. H. & Waters, S. L. 2005 Steady flows in pipes with finite curvature. *Phys. Fluids* **17**, 077102.

Smith, F. T. 1975 Pulsatile flow in curved pipes. *J. Fluid Mech.* **71**, 15–42.

Steinman, D. A. 2002 Image-based computational fluid dynamics modeling in realistic arterial geometries. *Ann. Biomed. Engng* **30**, 483–497.

Stuart, J. T. 1966 Double boundary layers in oscillatory viscous flows. *J. Fluid Mech.* **24**, 673–687.

Sudo, K., Sumida, M. & Yamane, R. 1992 Secondary motion of fully developed oscillatory flow in a curved pipe. *J. Fluid Mech.* **237**, 189–208.

Sugawara, M., Kajiya, F., Kitabatake, A. & Matsuo, H. 1989 *Blood Flow in the Heart and Large Vessels*. Springer.

Swanson, C. J., Stalp, S. R. & Donnelly, R. J. 1993 Experimental investigation of periodic flow in curved pipes. *J. Fluid Mech.* **256**, 69–83.

Tada, S., Oshima, S. & Yamane, R. 1996 Classification of pulsating flow patterns in curved pipes. *Trans. ASME* K: *J. Biomech. Engng* **118**, 311–317.

Truesdell, L. C. & Adler, R. J. 1970 Numerical treatment of fully developed laminar flow in helically coiled tubes. *AIChE J.* **16**, 1010–1015.

Winters, K. H. 1987 A bifurcation study of laminar flow in a curved tube of rectangular cross-section. *J. Fluid Mech.* **180**, 343–369.

Zabielski, L. & Mestel, A. J. 1998*a* Steady flow in a helically symmetric pipe. *J. Fluid Mech.* **370**, 297–320.

Zabielski, L. & Mestel, A. J. 1998*b* Unsteady blood flow in a helically symmetric pipe. *J. Fluid Mech.* **370**, 321–345.